# SECOND-MOMENT TURBULENCE MODEL
# OF FLOW THROUGH A ROTATING
# ANNULAR SEAL

By

WALLACE EDWARD WILCOX

Bachelor of Science

University of Missouri-Rolla

Rolla, Missouri

Submitted to the Faculty of the
Graduate College of the
Oklahoma State University
in partial fulfillment of
the requirements for
the Degree of
MASTER OF SCIENCE
May 1997

# SECOND-MOMENT TURBULENCE MODEL
# OF FLOW THROUGH A ROTATING
# ANNULAR SEAL

Thesis approved:

Thesis Advisor

David G. Lilley.

Thomas C. Collins

Dean of Graduate College

# ACKNOWLEDGMENTS

I would like to express my gratitude to Dr. Frank W. Chambers for his instruction and patience in assisting me in this project. His instruction in my first two graduate courses cultivated my interest in turbulence modeling. His willingness to assist at anytime and excellent attitude have made this project that much easier. I would also like to thank Dr. Lilley and Dr. Arena for their participation on my committee and their suggestions for improvement of this paper.

I express my utmost appreciation to Dr. George Huang of the University of Kentucky for his patience and enormous assistance to a person he has never met. His counseling has certainly been the difference in the development of this thesis. I would also like to thank Dr. Michael Leschziner of the University of Manchester Institute of Science and Technology for his Trans-Atlantic assistance that was very crucial. Also, I would like to state my appreciation to Dr. Gerald Morrisson of Texas A&M University for his willingness to supply both experimental data as well as insight into its meaning.

Finally, I would like to express my deepest gratitude to my wife, Angie, and our three daughters, Lauren, Bailey, and Allie. They have patiently provided support for my work and gone without a husband and father on countless weekends.

# TABLE OF CONTENTS

I. Introduction

II. Numerical Method

II. Results and Discussion

IV. Conclusions and Recommendations

# LIST OF TABLES

# LIST OF FIGURES

# NOMENCLATURE

| | |
|---|---|
| a | used to represent contributions of convection and diffusion in linearized transport equations |
| C | constant |
| c | clearance in the seal, 1.27 mm |
| E | constant equal to 9.7 |
| k | turbulent kinetic energy |
| n | normal distance from rotor surface |
| P | pressure |
| $P_e$ | Peclet number |
| $P_{ij}$ | Production of turbulent kinetic energy |
| pp | pressure perturbation variable in SIMPLE method |
| R | Radius of rotating shaft |
| r | radial variable |
| $r_v^+$ | non-dimensional wall variable |
| Re | Reynolds number |
| $S_U$ | linearized source term |
| $S_P$ | linearized source term, multiplied by $\phi$ |
| Ta | Taylor number=$(\omega c/V)*(c/R)^{0.5}$ |

| | |
|---|---|
| $U$ | axial mean velocity |
| $u'$ | fluctuating axial velocity |
| $\overline{u^2}$ | axial Reynolds normal stress |
| $\overline{uv}$ | axial-radial Reynolds shear stress |
| $\overline{uw}$ | axial-azimuthal Reynolds shear stress |
| $V$ | radial mean velocity |
| $v'$ | fluctuating radial velocity |
| $\overline{v^2}$ | radial Reynolds normal stress |
| $\overline{vw}$ | radial-azimuthal Reynolds shear stress |
| $W$ | azimuthal mean velocity |
| $w'$ | fluctuating azimuthal velocity |
| $\overline{w^2}$ | azimuthal Reynolds normal stress |
| $x$ | axial variable |
| (1) | Used to reference equation numbers in text |

**Greek Symbols**

| | |
|---|---|
| $\alpha$ | under-relaxation constant |
| $\Delta$ | dimensional variable |
| $\delta_{ij}$ | del operator($=1$ for $i=j$, $=0$ for $i\neq j$) |
| $\Sigma$ | summation |
| $\varepsilon$ | turbulent dissipation |
| $\phi$ | azimuthal variable, also used to represent many different variables |

| | |
|---|---|
| $\Gamma$ | diffusion coefficient |
| $\kappa$ | constant in wall functions, = 0.42 |
| $\lambda$ | constant used in inlet boundary condition for dissipation |
| $\mu$ | absolute viscosity |
| $\nu$ | kinematic viscosity |
| $\rho$ | fluid density |
| $\tau$ | shear stress |
| $\omega$ | shaft speed |

**Subscripts**

| | |
|---|---|
| 11 | axial component in axial direction |
| 12 | axial component in radial direction |
| 21 | radial component in axial direction |
| 22 | radial component in radial direction |
| 31 | azimuthal component in axial direction |
| 32 | azimuthal component in radial direction |
| 33 | azimuthal component in azimuthal direction |
| xx | same as 11 |
| xr | same as 12 |
| rx | same as 21 |
| rr | same as 22 |
| zx | same as 31 |

| | |
|---|---|
| zr | same as 32 |
| zz | same as 33 |
| E | east |
| N | north |
| P | center grid point |
| S | south |
| W | west |
| w | wall |

# CHAPTER I

# INTRODUCTION

## 1.1 Description of annular seals

Annular seals are widely used in industry to seal a fluid between a stationary and rotating member. They are commonly used in pumps in all types of industry to prevent recirculation inside the pump casing. Figure 1.1 below shows a typical multi-stage pump that has several examples of annular seals. Annular seals between the pump casing and the impeller are termed "wear rings" and those located directly on the pump shaft are simply described as "bushings".

The amount of leakage that passes through the seals can greatly impact the performance of the pump. As the seals wear and open up they can cause so much recirculation that the pump overloads the driver. The need to reduce the amount of leakage requires that the clearance between the stationary and rotating members be kept at the absolute minimum. Since large pressure drops sometimes exist across seals 3.5 MPa[500 psi], very high velocities exist within the seals[2].

The small clearances seen in many seals (0.127 mm [0.005 in] for a 63.5 mm[2.5 in] diam seal) and large pressure drops may cause the seals to act as hydrodynamic bearings (see Figure 1.2). This can be both beneficial as well as detrimental to the operation of the pump. Additional "bearings" in the center of a long multi-stage pump as seen in Figure 1.1 are a necessity to support the shaft due to the high tangential loads inflicted by the impellers. However, if these "bearings" have the wrong internal stiffness due to very high velocities (see Figure 1.2), the rotordynamic stability of the pump can be greatly effected. The internal stiffness and dampening of a seal can be calculated if the pressure and velocity profiles are known. A representation of the linkage between the fluid velocities, pressures, and hydrodynamic characteristics is shown in (1) below [2,3,37].

Figure 1.1. Cross-section of 10 stage centrifugal pump

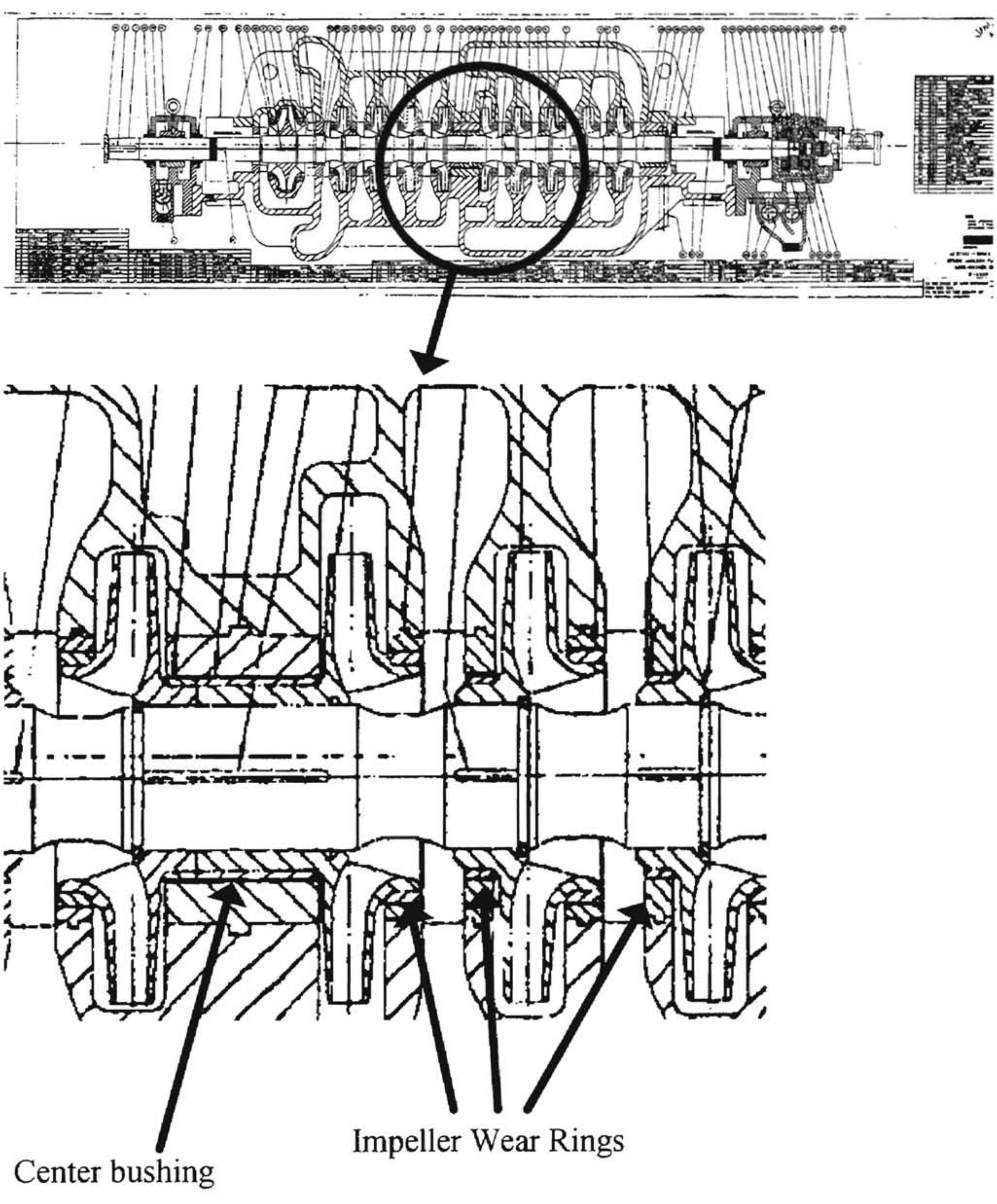

Figure 1.2. Representation of fluid stiffness and dampening in an annular seal

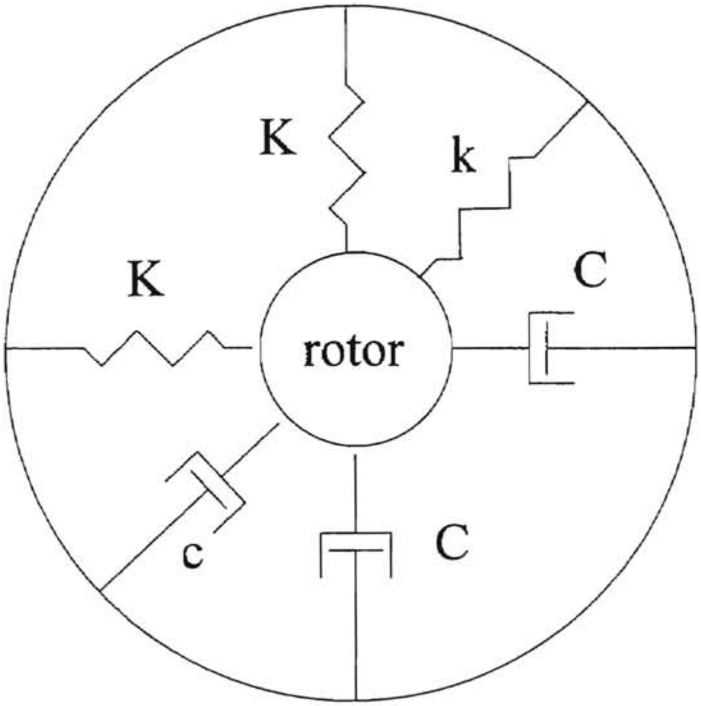

$$\begin{bmatrix} F_X \\ F_Y \end{bmatrix} = \begin{bmatrix} K & k \\ -k & K \end{bmatrix} \begin{bmatrix} z \\ y \end{bmatrix} + \begin{bmatrix} C & c \\ -c & C \end{bmatrix} \begin{bmatrix} W \\ V \end{bmatrix} \qquad (1)$$

where $F_x$ and $F_Y$ are functions of the pressure profile inside the seal.

### 1.2 Methods used to calculate pressure and velocity profiles in annular seals

There are many different methods to calculate the pressure and velocity profiles in annular seals. They can be divided into two different groups. The first is a two dimensional method with the addition of swirl velocity. The second is a three dimensional computational method that allows for changes in the azimuthal direction[2].

The flow is highly turbulent with leakage Reynolds numbers in excess of 15,000 in most cases. Both two and three dimensional models require additional equations to model the flow besides the equations of continuity and momentum.

#### 1.2.1 Two dimensional methods

Two dimensional models use the governing equations of continuity and momentum to solve the velocity and pressure profiles. They solve for all three velocity components (U, V, and W), but limit the changes with direction to the axial and radial direction only (i.e. $\frac{\partial}{\partial\phi} = 0$). They are based on the assumption that the inner rotating cylinder is centered inside the outer stationary cylinder[37].

#### 1.2.2 Three dimensional methods

The three dimensional models are much more complex because they allow for variations in the azimuthal direction. This eliminates the need for the centered annulus assumption. However, this method is quite difficult to model because the equilibrium position of the shaft must be constantly calculated, which requires the inner boundary to move throughout the computation. This is usually accomplished by having the coordinate system rotate with the shaft at a fixed speed, ω[3].

### 1.3 Numerical approximation of Reynolds stresses

Computation of the time varying velocity components (i.e U(x,r,z,t)) for this type of flow is not feasible due to the enormous amount of computational time and memory required. For this reason the velocity components are broken down into a mean and fluctuating value (u = U+ u'). Substitution of the mean and fluctuating components into the conservation of continuity and momentum equations along with time averaging produces the Reynolds equations, see (2),(3), and (4) below[10,38].

$$\frac{\partial U}{\partial x} + \frac{\partial V}{\partial r} + \frac{\partial W}{\partial z} = 0 \qquad (2)$$

$$\rho \frac{DV}{Dt} = -\nabla P + \nabla \bullet \tau_{ij} \qquad (3)$$

where

$$\tau_{ij} = \mu\left(\frac{\partial U_i}{\partial x_j} + \frac{\partial U_j}{\partial x_i}\right) - \rho\overline{u'_i\, u'_j} \qquad (4)$$

The second term on the right side of (4) is the product of the velocity fluctuations and is termed the Reynolds stress. The numerical methods to solve for the Reynolds stresses are called turbulence models. The types of turbulent models can be broken down into groups that include: eddy viscosity, Algebraic stress, and Reynolds stress models.

The eddy viscosity models are based upon the Boussinesq assumption that the turbulent stresses can be approximated as the product of the eddy viscosity and the mean strain, see (5). By far, the most popular eddy viscosity model is a two equation model, called k-ε, which approximates the eddy viscosity as a function of the turbulent kinetic energy and dissipation[38]. Eddy viscosity methods have been proven to be lacking due to their inability to resolve normal-stress anisotropy, especially in swirling and/or recirculating flows[6].

$$\tau_{ij} = -\rho\overline{u_i u_j} = \mu_{turb}\left(\frac{\partial U}{\partial r} + \frac{\partial V}{\partial x}\right) \tag{5}$$

k-ε model

$$\mu_{turb} = C_\mu \rho \frac{k^2}{\varepsilon} \tag{6}$$

Algebraic stress models are located between eddy viscosity and Reynolds stress models in both difficulty and accuracy[6]. They approximate the convective and diffusive components of the stress transport equation with an algebraic expression that represents them as a function of the turbulent kinetic energy, see (7) and (8) below. Each Reynolds stress is calculated from an algebraic equation. The only differential transport equations are for the turbulent kinetic energy and dissipation. (6) is still used for the eddy viscosity; however, the Reynolds stresses are calculated and substituted into the momentum equations, see (9) and (10) below [11,32].

Diffusion

$$\frac{\partial}{\partial x_k}\left(c_s \frac{k}{\varepsilon}\overline{u_k u_l}\frac{\partial \overline{u_i u_j}}{\partial x_l}\right) = C_K\left[(1+\alpha)\frac{\overline{u_i u_j}}{k} - \alpha\frac{2}{3}\delta_{ij}\right] \tag{7}$$

Convection

$$\frac{\partial U_k \overline{u_i u_j}}{\partial x_k} = D_K\left[(1+\beta)\frac{\overline{u_i u_j}}{k} - \beta\frac{2}{3}\delta_{ij}\right] \tag{8}$$

where $C_k$, $D_k$, $\alpha$, and $\beta$ are constants determined by the type of flow.

$$\rho\overline{u^2} = \frac{2}{3}\rho k - 2\mu_{eff}\frac{\partial U}{\partial x} \tag{9}$$

$$\rho\overline{uv} = -\mu_{eff}\left(\frac{\partial U}{\partial r} + \frac{\partial V}{\partial x}\right) \tag{10}$$

Reynolds stress turbulence models have transport equations for each of the six Reynolds stresses, $\tau_{ij}$, instead of approximating them as a function of the mean strain or turbulence energy[19].

$$\frac{\partial U_k \overline{u_i u_j}}{\partial x_k} = \frac{\partial}{\partial x_k}\left(c_s\frac{k}{\varepsilon}\overline{u_k u_l}\frac{\partial \overline{u_i u_j}}{\partial x_l}\right) + P_{ij} - \frac{2}{3}\delta_{ij}\varepsilon - c_1\varepsilon\left(\frac{\overline{u_i u_j} - \frac{2}{3}\delta_{ij}k}{k}\right) - c_2\left(P_{ij} - \frac{1}{3}\delta_{ij}P_{kk}\right) \tag{11}$$

Approximations are made for the pressure-strain and third order correlations, but the convection terms are exact. They are much more complicated to calculate but have exhibited better performance than both the eddy viscosity and algebraic stress models especially in swirling/recirculating flows[6,23]. For example, the convection term for the $\overline{uv}$ equation in the Algebraic stress model is represented by

$$C_{12} = \rho\frac{\overline{uv}}{k}\left(U\frac{\partial k}{\partial x} + V\frac{\partial k}{\partial y}\right) \tag{12}$$

Note, that it is entirely independent of the swirl velocity W. The exact convection term, as calculated in the Reynolds stress model is shown below:

$$C_{12} = \rho U \frac{\partial \overline{uv}}{\partial x} + \rho V \frac{\partial \overline{uv}}{\partial r} - \rho \overline{uw} \frac{W}{r} \qquad (13)$$

## 1.4 Previous computational and experimental work

### 1.4.1 Work of Stoff

In 1980, Stoff[36] modeled the flow of an incompressible fluid through a labyrinth seal with a cavity Reynolds number of 30,000 and a Taylor number of 12,000 using the SIMPLE[29] method for the mean velocity equations and a k-ε turbulence model. This study was made using the assumption of a centered annulus, i.e. 2-D with swirl velocity. The main objective of this study was to estimate the leakage through the labyrinth seal. Overall, the model predicted the leakage rate well. No comparisons were made to the turbulence quantities because this was not the objective of the work. Likewise, they were not available from the computational model.

### 1.4.2 Work of Demko

In 1986, Demko[4] modeled the flow of an incompressible fluid through a labyrinth for several different leakage rates, which gave a Reynolds range of 33,000 -55,000 and a Taylor(Ta) number range of 0 to 19,000. The computational model used the QUICK[21] differencing algorithm and a k-ε turbulence model. He compared his computational data against hot-film experimental data. His model did a good job of predicting the axial and azimuthal velocity profiles, but overpredicted the turbulent kinetic energy profiles past the labyrinth teeth in the cavity, especially at higher Reynolds and Taylor numbers. No comparisons were made to Reynolds stresses because they were not available from the computational model.

### 1.4.3 Work of Dietzen and Nordmann

In 1987, Dietzen and Nordmann[3] modeled incompressible flow through an annular seal using a perturbation solution. This study did not assume a centered annulus and was comprised of a full 3-D solution with a k-ε turbulence model. A rotating coordinate system was used that turned at the rotational speed of the shaft. This model produced rotordynamic coefficients, see (1), that agreed closely with experimental data.

### 1.4.4 Work of Morrison, et al.

In 1991, Morrison, et al.[27] conducted 3-D laser Doppler anemometer measurements inside an annular seal (see Figure 1.3 below). The rotor was rotated at 3600 rpm which results in a Taylor number of 4500 and an azimuthal velocity for the rotor surface of 28.7 m/s. For the leakage rate of 4.86 kg/s, the leakage Reynolds number is 18,600 with an average axial mean velocity of 7.3 m/s. Both the Reynolds and Taylor numbers are well within normal operating values obtained in production turbomachinery. The ratio of rotor speed to average leakage velocity is 3.9. Velocity and Reynolds stress data was provided in both graphical and tabular format.

Figure 1.3. Experimental setup of Morrison, et al.[27]

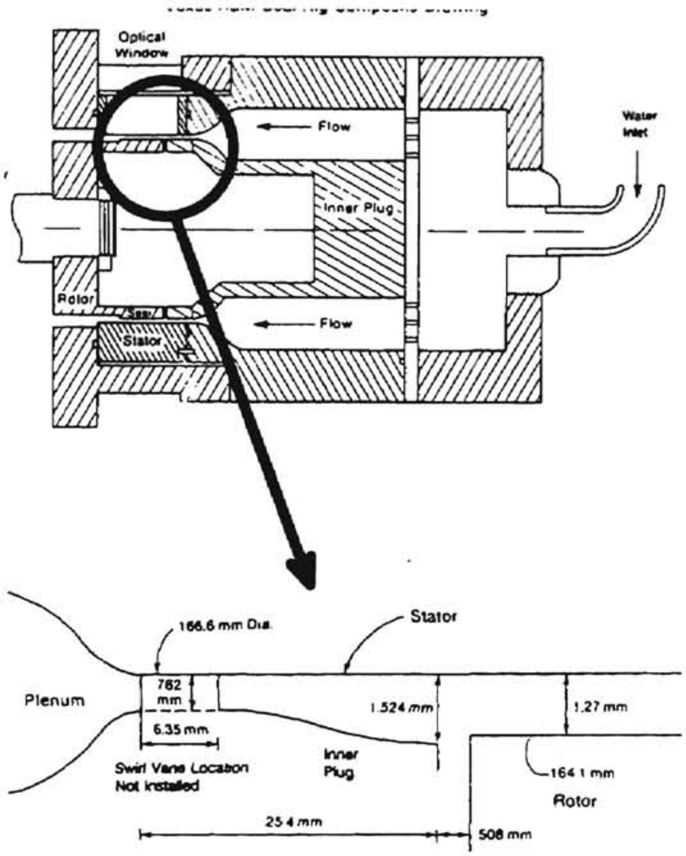

### 1.4.5 Work of Rhode

In 1993, Rhode[32] used a full three dimensional model which contained a modified bipolar coordinate system, QUICK differencing scheme, and k-ε turbulence model to simulate compressible flow through a labyrinth seal. Due to the large computational requirements, the computational domain consisted of only one labyrinth cavity. The shaft speed was 7000 rpm and the whirl orbit frequency was 3500 cpm. The working fluid was air at 3.0 atm and 294 K. The axial Reynolds number was 19,200. The calculated rotordynamic coefficients compared favorably against experimental measurements.

## 1.5 Objective

All of the previous computational work for flow through seals in turbomachinery utilized an eddy viscosity turbulence model of some type. Due to the largely anisotropic nature of the flow and the inability of the eddy viscosity models to predict anisotropic turbulence, the objective of this research is to apply an existing Reynolds stress turbulence model to the flow geometry of a rotating annular seal.

## 1.6 Description of computational model

A computational model, based on the SIMPLE[29] and TEAM[11] methods, is developed to simulate the flow of water through a rotating annular seal. The annular seal is geometrically represented by a cylindrical annulus in which the inner cylinder rotates at a fixed speed and has a forward facing step as illustrated in Figure 1.4 below. A computer code is written in C that uses a staggered grid method for the continuity, momentum, and Reynolds stress equations. Reynolds stress turbulence models can produce instabilities in the iterative calculation process if they are substituted directly into the Reynolds equation, see (3) above. These instabilities are avoided by representing each stress as a function of the mean strain as well as an additional source term. This creates an "apparent" viscosity term in the momentum equations that is numerically forced to be positive at all times to prevent the solution from diverging[11]. The computed data is compared against mean flow and turbulence data obtained from the laser Doppler anemometer experiment of Morrison, et al.[27]. The inlet conditions to the computational model are provided from the experimental data.

Figure 1.4. Computational geometry

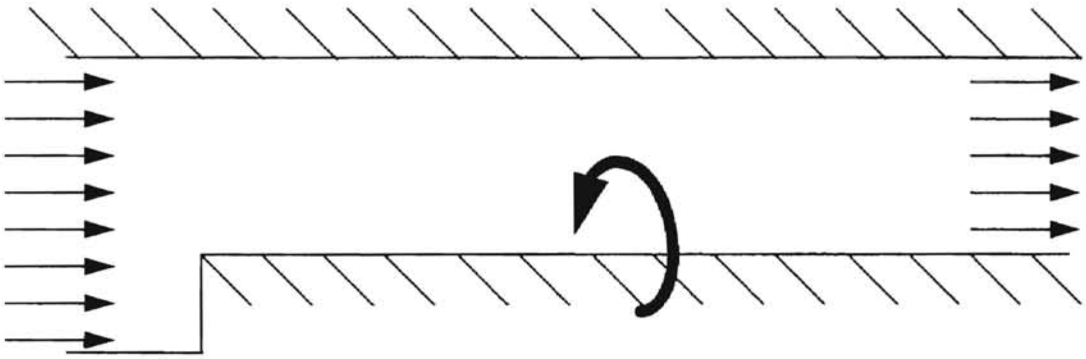

# CHAPTER II

# NUMERICAL METHOD

## 2.1 Governing Equations

The governing equations for the fluid flow through the seal are the time averaged continuity, momentum, and turbulence transport equations. The governing equations for the flow model are simplified by assuming incompressible ($\rho$=constant), steady state conditions($\partial/\partial t=0$). Likewise the axisymmetric condition allows the equations to be reduced to two dimensions ($\partial/\partial\phi=0$) with three velocity components.

### 2.1.1 Continuity and Momentum Equations

The time averaged incompressible continuity and momentum equations for the mean flow quantities (U,V, and W) in cylindrical polar coordinates are given below.

$$\frac{\partial(rU)}{\partial x}+\frac{\partial(rV)}{\partial r}=0 \tag{14}$$

$$U\frac{\partial U}{\partial x}+V\frac{\partial U}{\partial r}=-\frac{1}{\rho}\frac{\partial P}{\partial x}+\frac{\partial}{\partial x}\nu\frac{\partial U}{\partial x}+\frac{\partial}{\partial r}\frac{\nu}{r}\frac{\partial U}{\partial r}+\frac{\nu}{r}\frac{\partial V}{\partial r}-\frac{\partial\overline{u^2}}{\partial x}-\frac{1}{r}\frac{\partial r\,\overline{uv}}{\partial r} \tag{15}$$

$$\begin{aligned}V\frac{\partial V}{\partial x}+V\frac{\partial V}{\partial r}-\frac{W^2}{r}&=-\frac{1}{\rho}\frac{\partial P}{\partial r}+\frac{\partial}{\partial x}\nu\frac{\partial V}{\partial x}+\\ \frac{\partial}{\partial r}\frac{\nu}{r}\frac{\partial V}{\partial r}+\frac{\nu}{r}\frac{\partial V}{\partial r}-\frac{\nu V}{r^2}&-\frac{\partial\overline{uv}}{\partial x}-\frac{1}{r}\frac{\partial r\,\overline{v^2}}{\partial r}+\frac{\overline{w^2}}{r}\end{aligned} \tag{16}$$

$$U\frac{\partial W}{\partial x}+V\frac{\partial W}{\partial r}+\frac{VW}{r}=+\frac{\partial}{\partial x}\nu\frac{\partial W}{\partial x}+\frac{\partial}{\partial r}\frac{\nu}{r}\frac{\partial W}{\partial r}$$
$$+\frac{\nu}{r}\frac{\partial W}{\partial r}+\frac{W}{r}\frac{\partial \nu}{\partial r}-\frac{\nu W}{r^2}-\frac{\partial\overline{uw}}{\partial x}-\frac{1}{r}\frac{\partial r\,\overline{vw}}{\partial r}+\frac{\overline{vw}}{r} \tag{17}$$

These are the equations that govern the mean flow quantities (U,V,W, and P). However, since the products of the fluctuating velocities ($\overline{u^2}$, $\overline{v^2}$, $\overline{uv}$, $\overline{w^2}$, $\overline{uw}$, and $\overline{vw}$) are unknown, these equations are not a closed set. These unknown terms are called Reynolds stresses. An additional set of six transport equations is required for the solution of the Reynolds stress terms.

### 2.1.2 Reynolds Stress Transport Equations

The Reynolds stresses mentioned in section 2.1.1 are solved by using the Reynolds stress transport equation [22,31] for each individual stress (shown below in tensor notation):

$$\underbrace{\frac{\partial U_k\,\overline{u_i u_j}}{\partial x_k}}_{\text{Convection}}=\underbrace{\frac{\partial}{\partial x_k}\left(c_s\frac{k}{\varepsilon}\overline{u_k u_l}\frac{\partial\overline{u_i u_j}}{\partial x_l}\right)}_{\text{Diffusion}}\underbrace{+P_{ij}}_{\text{Prod-uction}}\underbrace{-\frac{2}{3}\delta_{ij}\varepsilon}_{\text{Dissi-pation}}\underbrace{-c_1\,\varepsilon\left(\frac{\overline{u_i u_j}-\frac{2}{3}\delta_{ij}\,k}{k}\right)-c_2\left(P_{ij}-\frac{1}{3}\delta_{ij}\,P_{kk}\right)}_{\text{Re-distribution}}$$

where production is exact and is defined as

$$P_{ij}=-\overline{u_i u_k}\frac{\partial U_j}{\partial x_k}-\overline{u_j u_k}\frac{\partial U_i}{\partial x_k} \tag{19}$$

and $\delta_{ij}=1$ for i=j, and $\delta_{ij}=0$ for i≠j.

The model is closed with the introduction of the turbulence-energy dissipation ($\varepsilon$) transport equation.

$$U_k \frac{\partial \varepsilon}{\partial x_k} = \frac{\partial}{\partial x_k}\left( c_s \frac{k}{\varepsilon} \overline{u_k u_l} \frac{\partial \varepsilon}{\partial x_l} \right) + c_{\varepsilon 1} \frac{\varepsilon}{k} P_{kk} - c_{\varepsilon 1} \frac{\varepsilon^2}{k} \tag{20}$$

These seven additional equations along with the continuity and momentum equations from 2.1.1 form a closed set of eleven equations and eleven unknowns. The constants in the models above are recommened to be the values shown below in Table 2.1 [11,19,31] .

Table 2.1. Turbulence transport equation constants

| $C_1$ | $C_2$ | $C_{\varepsilon 1}$ | $C_{\varepsilon 2}$ | $C_{\varepsilon 3}$ | $C_S$ |
|---|---|---|---|---|---|
| 1.8 | 0.6 | 1.44 | 1.9 | 1.16 | 0.22 |

## 2.2 Finite Difference Equations

All of the above equations can be represented in the following common form:

$$\begin{aligned} &\frac{\partial}{\partial x}(rU\phi) + \frac{\partial}{\partial r}(rV\phi) = \frac{\partial}{\partial x}\left( r\,\Gamma_{XX}\, U \frac{\partial \phi}{\partial x}\right) + \frac{\partial}{\partial r}\left( r\,\Gamma_{YY}\, U \frac{\partial \phi}{\partial r}\right) \\ &+ \frac{\partial}{\partial x}\left( r\,\Gamma_{XY}\, U \frac{\partial \phi}{\partial r}\right) + \frac{\partial}{\partial r}\left( r\,\Gamma_{YY}\, U \frac{\partial \phi}{\partial x}\right) + S_U r + S_P\,\phi\, r \end{aligned} \tag{21}$$

where $\phi$=1(continuity), U, V, W, $\overline{u^2}$, $\overline{v^2}$, $\overline{w^2}$, $\overline{uv}$, $\overline{uw}$, $\overline{vw}$, and $\varepsilon$ . The $S_U$ and $S_P$ terms represent the linearized source term of each equation. The finite difference equations for each $\phi$ are obtained by integrating (21) over each control volume and approximating each differential with a Taylor series expansion. This results in an expression for each node point in terms of the neighboring grid point values of the form:

$$a_E\phi_E + a_W\phi_W + a_N\phi_N + a_S\phi_S + S_U = a_P\phi_P \tag{22}$$

where $a_E = U\phi - \Gamma\phi \frac{\partial \phi}{\partial x}$ , along the eastern boundary of the control volume and $a_P = a_E + a_W + a_N + a_S - S_P$. The solution procedure for the U,V,W, and P values is based on the SIMPLE method[29]. Formulas for $\Gamma_\phi$, $S_u$, and $S_p$ for all of the variables are given below in Tables 2.2 and 2.3[11,34]:

Table 2.2. Diffusion coefficients for transport equations

| $\phi$ | $\Gamma_{xx}$ | $\Gamma_{yy}$ | $\Gamma_{xy}$ | $\Gamma_{yx}$ |
|---|---|---|---|---|
| U | $\nu_l + \nu_{11}$ | $\nu_l + \nu_{12}$ | 0 | 0 |
| V | $\nu_l + \nu_{21}$ | $\nu_l + \nu_{22}$ | 0 | 0 |
| W | $\nu_l + \nu_{31}$ | $\nu_l + \nu_{32}$ | 0 | 0 |
| $\overline{u^2}$ | $\nu_l + c_s \frac{k}{\varepsilon}\overline{u^2}$ | $\nu_l + c_s \frac{k}{\varepsilon}\overline{v^2}$ | $c_s \frac{k}{\varepsilon}\overline{uv}$ | $c_s \frac{k}{\varepsilon}\overline{uv}$ |
| $\overline{v^2}$ | $\nu_l + c_s \frac{k}{\varepsilon}\overline{u^2}$ | $\nu_l + c_s \frac{k}{\varepsilon}\overline{v^2}$ | $c_s \frac{k}{\varepsilon}\overline{uv}$ | $c_s \frac{k}{\varepsilon}\overline{uv}$ |
| $\overline{w^2}$ | $\nu_l + c_s \frac{k}{\varepsilon}\overline{u^2}$ | $\nu_l + c_s \frac{k}{\varepsilon}\overline{v^2}$ | $c_s \frac{k}{\varepsilon}\overline{uv}$ | $c_s \frac{k}{\varepsilon}\overline{uv}$ |
| $\overline{uv}$ | $\nu_l + c_s \frac{k}{\varepsilon}\overline{u^2}$ | $\nu_l + c_s \frac{k}{\varepsilon}\overline{v^2}$ | $c_s \frac{k}{\varepsilon}\overline{uv}$ | $c_s \frac{k}{\varepsilon}\overline{uv}$ |
| $\overline{uw}$ | $\nu_l + c_s \frac{k}{\varepsilon}\overline{u^2}$ | $\nu_l + c_s \frac{k}{\varepsilon}\overline{v^2}$ | $c_s \frac{k}{\varepsilon}\overline{uv}$ | $c_s \frac{k}{\varepsilon}\overline{uv}$ |
| $\overline{vw}$ | $\nu_l + c_s \frac{k}{\varepsilon}\overline{u^2}$ | $\nu_l + c_s \frac{k}{\varepsilon}\overline{v^2}$ | $c_s \frac{k}{\varepsilon}\overline{uv}$ | $c_s \frac{k}{\varepsilon}\overline{uv}$ |
| $\varepsilon$ | $\nu_l + c_s \frac{k}{\varepsilon}\overline{u^2}$ | $\nu_l + c_s \frac{k}{\varepsilon}\overline{v^2}$ | $c_s \frac{k}{\varepsilon}\overline{uv}$ | $c_s \frac{k}{\varepsilon}\overline{uv}$ |

Table 2.3. Source terms for transport equations

| $\phi$ | $S_u$ | $S_p$ |
|---|---|---|
| $U$ | $-\frac{1}{\rho}\frac{\partial P}{\partial x}-\frac{\partial S_{xx}}{\partial x}-\frac{1}{r}\frac{\partial rS_{xy}}{\partial y}$ | $0$ |
| $V$ | $+\frac{W^2}{r}-\frac{1}{\rho}\frac{\partial P}{\partial y}-\frac{\partial S_{yx}}{\partial x}-\frac{1}{r}\frac{\partial rS_{yy}}{\partial y}+\frac{\overline{ww}}{r}$ | $\frac{\nu_1}{r^2}$ |
| $W$ | $-\frac{VW}{r}-\frac{\partial S_{zx}}{\partial x}-\frac{1}{r}\frac{\partial rS_{zy}}{\partial y}-\frac{\overline{vw}}{r}$ | $\frac{\nu_1}{r^2}$ |
| $\overline{u^2}$ | $(1-c_2)P_{11}+\frac{2}{3}c_2P_k+\frac{2}{3}(c_1-1)\varepsilon$ | $-c_1\frac{\varepsilon}{k}$ |
| $\overline{v^2}$ | $(1-c_2)P_{22}+\frac{2}{3}c_2P_k+\frac{2}{3}(c_1-1)\varepsilon+2\overline{vw}\frac{W}{r}+\frac{2c_sk}{\varepsilon}\frac{(\overline{w^2})^2}{r^2}$ | $-c_1\frac{\varepsilon}{k}+\frac{2c_sk}{\varepsilon}\frac{\overline{w^2}}{r^2}$ |
| $\overline{w^2}$ | $(1-c_2)P_{33}+\frac{2}{3}c_2P_k+\frac{2}{3}(c_1-1)\varepsilon-2\overline{vw}\frac{W}{r}+\frac{2c_sk}{\varepsilon}\frac{\overline{v^2}\,\overline{w^2}}{r^2}$ | $-c_1\frac{\varepsilon}{k}+\frac{2c_sk}{\varepsilon}\frac{\overline{w^2}}{r^2}$ |
| $\overline{uv}$ | $(1-c_2)P_{12}+\overline{uw}\frac{W}{r}$ | $-\frac{c_sk}{\varepsilon}$ |
| $\overline{uw}$ | $(1-c_2)P_{13}-\overline{u\,v}\frac{W}{r}$ | $-\frac{c_sk}{\varepsilon}$ |
| $\overline{vw}$ | $(1-c_2)P_{23}-(\overline{v^2}-\overline{w^2})\frac{W}{r}$ | $-\frac{c_sk}{\varepsilon}$ |
| $\varepsilon$ | $c_{\varepsilon 1}\frac{\varepsilon}{k}P_k$ | $-c_{\varepsilon 2}\frac{\varepsilon}{k}$ |

where

$$P_{11} = -2(\overline{uu}\frac{\partial U}{\partial x}+\overline{uv}\frac{\partial U}{\partial r}) \tag{23a}$$

$$P_{22} = -2(\overline{uv}\frac{\partial V}{\partial x}+\overline{v^2}\frac{\partial V}{\partial r}-\overline{vw}\frac{W}{r}) \tag{23b}$$

$$P_{33} = -2(\overline{u\,w}\frac{\partial W}{\partial x}+\overline{v\,w}\frac{\partial W}{\partial r}-\overline{w^2}\frac{V}{r}) \tag{23c}$$

$$P_{12} = -(\overline{u^2}\frac{\partial V}{\partial x}+\overline{v^2}\frac{\partial U}{\partial r}-\overline{u\,w}\frac{W}{r}-\overline{uv}\frac{V}{r}) \tag{23d}$$

$$P_{13} = -(\overline{u^2}\frac{\partial W}{\partial x}+\overline{uv}\frac{\partial W}{\partial r}+\overline{vw}\frac{\partial U}{\partial r}-\overline{u\,w}\frac{\partial V}{\partial r}) \tag{23e}$$

$$P_{23} = -(\overline{u\,v}\frac{\partial W}{\partial x} + \overline{v^2}\frac{\partial W}{\partial r} - \overline{vw}\frac{\partial U}{\partial x} + \overline{u\,w}\frac{\partial V}{\partial x} + \overline{w^2}\frac{W}{r}) \tag{23f}$$

The turbulence transport equations have an additional set of cross diffusion terms that only appear in cylindrical polar coordinates. These terms are added to the source term $S_{U,\phi}$ and are shown below in Table 2.4[34].

Table 2.4. Cross diffusion coefficients for turbulence quantities in cylindrical coordinates

| | |
|---|---|
| $\overline{u^2}$ | $\frac{1}{r}\frac{\partial}{\partial r}\left\{rC_s\frac{k}{\varepsilon}\overline{uv}\frac{\partial\overline{u^2}}{\partial x}\right\} + \frac{\partial}{\partial x}C_s\frac{k}{\varepsilon}\overline{uv}\frac{\partial\overline{u^2}}{\partial r}$ |
| $\overline{v^2}$ | $\frac{\partial}{\partial x}C_s\frac{k}{\varepsilon}(\overline{uv}\frac{\partial\overline{v^2}}{\partial r} - 2\overline{uw}\frac{\overline{vw}}{r}) + \frac{1}{r}\frac{\partial}{\partial r}\left\{rC_s\frac{k}{\varepsilon}(\overline{uv}\frac{\partial\overline{v^2}}{\partial x} - 2\frac{(\overline{vw})^2}{r})\right\} -$<br>$\frac{2}{r}C_s\frac{k}{\varepsilon}\left\{\overline{uw}\frac{\partial\overline{vw}}{\partial x} + \overline{vw}\frac{\partial\overline{vw}}{\partial r} + \overline{w^2}(\frac{\overline{v^2} - \overline{w^2}}{r})\right\}$ |
| $\overline{w^2}$ | $\frac{\partial}{\partial x}C_s\frac{k}{\varepsilon}(\overline{uv}\frac{\partial\overline{w^2}}{\partial r} + 2\overline{uw}\frac{\overline{vw}}{r}) + \frac{1}{r}\frac{\partial}{\partial r}\left\{rC_s\frac{k}{\varepsilon}(\overline{uv}\frac{\partial\overline{w^2}}{\partial x} + 2\frac{(\overline{vw})^2}{r})\right\} +$<br>$\frac{2}{r}C_s\frac{k}{\varepsilon}\left\{\overline{uw}\frac{\partial\overline{vw}}{\partial x} + \overline{vw}\frac{\partial\overline{vw}}{\partial r} + \overline{w^2}(\frac{\overline{v^2} - \overline{w^2}}{r})\right\}$ |
| $\overline{uv}$ | $\frac{\partial}{\partial x}C_s\frac{k}{\varepsilon}(\overline{uv}\frac{\partial\overline{uv}}{\partial r} - \frac{(\overline{uw})^2}{r}) + \frac{1}{r}\frac{\partial}{\partial r}\left\{rC_s\frac{k}{\varepsilon}(\overline{uv}\frac{\partial\overline{uv}}{\partial x} - \overline{vw}\frac{\overline{uw}}{r})\right\} +$<br>$\frac{1}{r}C_s\frac{k}{\varepsilon}\left\{\overline{uw}\frac{\partial\overline{uw}}{\partial x} + \overline{vw}\frac{\partial\overline{uw}}{\partial r} + \overline{w^2}\frac{\overline{uv}}{r}\right\}$ |
| $\overline{uw}$ | $\frac{\partial}{\partial x}C_s\frac{k}{\varepsilon}(\overline{uv}\frac{\partial\overline{uw}}{\partial r} + \overline{uw}\frac{\overline{uv}}{r}) + \frac{1}{r}\frac{\partial}{\partial r}\left\{rC_s\frac{k}{\varepsilon}(\overline{uv}\frac{\partial\overline{uw}}{\partial x} + \overline{vw}\frac{\overline{uv}}{r})\right\} +$<br>$\frac{1}{r}C_s\frac{k}{\varepsilon}\left\{\overline{uw}\frac{\partial\overline{uv}}{\partial x} + \overline{vw}\frac{\partial\overline{uv}}{\partial r} - \overline{w^2}\frac{\overline{uw}}{r}\right\}$ |

| | |
|---|---|
| $\overline{vw}$ | $\frac{\partial}{\partial x} C_s \frac{k}{\varepsilon} (\overline{uv} \frac{\partial \overline{vw}}{\partial r} + \overline{uw} \frac{\overline{v^2} - \overline{w^2}}{r}) + \frac{1}{r} \frac{\partial}{\partial r} \left\{ r C_s \frac{k}{\varepsilon} (\overline{uv} \frac{\partial \overline{vw}}{\partial x} + \overline{vw} \frac{\overline{v^2} - \overline{w^2}}{r}) \right\} +$<br>$\frac{1}{r} C_s \frac{k}{\varepsilon} \left\{ \overline{uw} \frac{\partial}{\partial x} (\overline{v^2} - \overline{w^2}) + \overline{vw} \frac{\partial}{\partial r} (\overline{v^2} - \overline{w^2}) - 4\overline{w^2} \frac{\overline{vw}}{r} \right\}$ |

### 2.2.1 Approximation of convection/diffusion operator

The convective and diffusion terms in (21) cannot be represented by a central, forward, or backward difference approximation alone. The physical characteristics of the flow require that sometimes the convective contributions upwind of a particular grid point affect it more than those downwind. The convective and diffusive terms are represented by the power law scheme which is a combination of the upwind differencing and exponential methods. It provides better representation of the non-linear effects than the hybrid scheme which is a combination of upwind and central differencing (see Figure 2.1 below). The power law scheme is outlined below for the range of Peclet (Pe) numbers [29].

For $P_e < -10$

$$a_E = -P_e * D_e$$

for $-10 <= P_e <= 0$

$$a_E = \{ (1+0.1*P_e)^5 - P_e \} * D_e$$

for $0 <= Pe <= 10$

$$a_E = (1 - 0.1*P_e)5*D_e$$

for $P_e > 10$

$$a_E = 0$$

where $D_e = \frac{\Gamma}{dx}$, and $Pe = \frac{\rho U(dx)}{\Gamma}$ = ratio of convection/diffusion

Figure 2.1. Approximations of convection/diffusion operator[29]

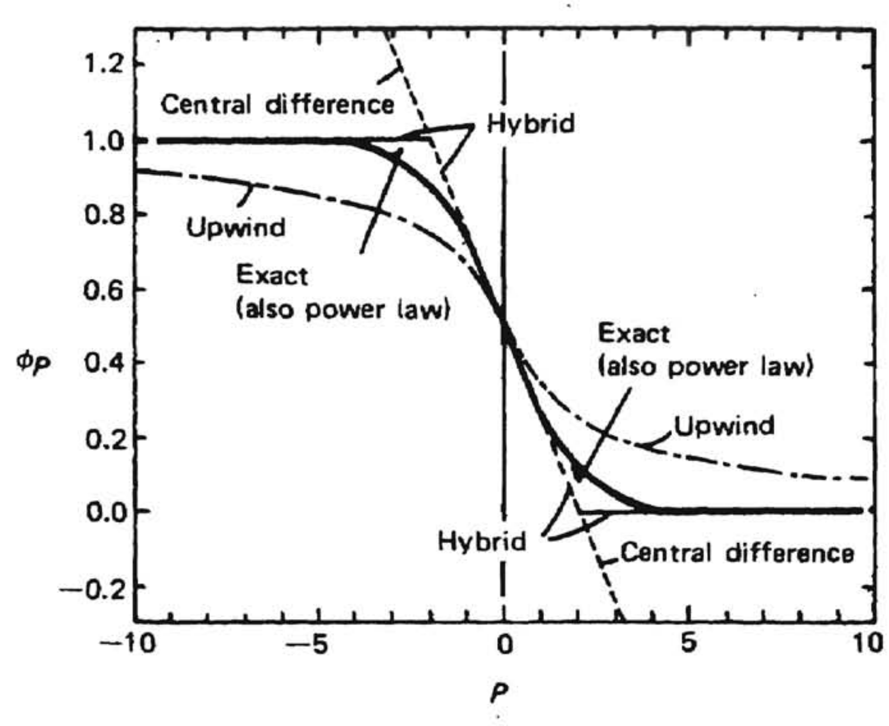

## 2.3 Grid System

A staggered grid system is used for both the mean quantities as well as the turbulence quantities. Note that the U velocity is staggered in the horizontal direction only (Figure 2.2), likewise the V velocity is staggered in the vertical direction only (Figure 2.3). The normal turbulence stresses are centered, but the shear stresses are all staggered. The $\overline{uv}$ stress is staggered in both the horizontal and vertical directions. The control volumes for the $\overline{uw}$ and $\overline{vw}$ stresses are the same as those for the U and V velocities respectively(see Figure 2.4)[11,22,29].

The staggered grid for the mean flow quantities is required so that the continuity equation will produce a realistic velocity field [29]. It also allows the U velocity to be defined directly on both the inlet western and outlet eastern boundaries.

The staggered location of the turbulence quantities allows the largest mean strain production term for each to be calculated without interpolating. Likewise, the contributions from each Reynolds stress to the momentum equations can be made with less interpolation. This will be discussed in more detail in later sections.

Figure 2.2. U momentum cell (control volume)

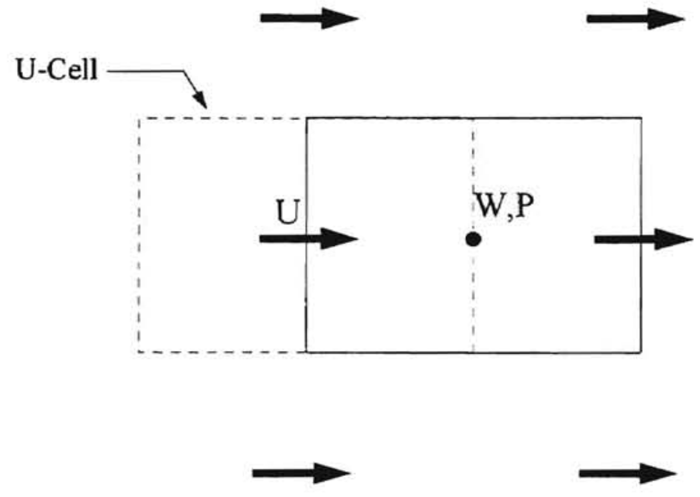

Figure 2.3. V momentum cell (control volume)

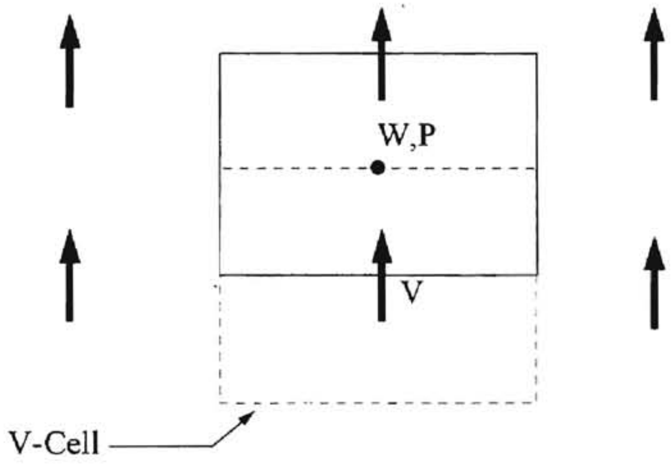

Figure 2.4. Reynolds stress cell (control volume)

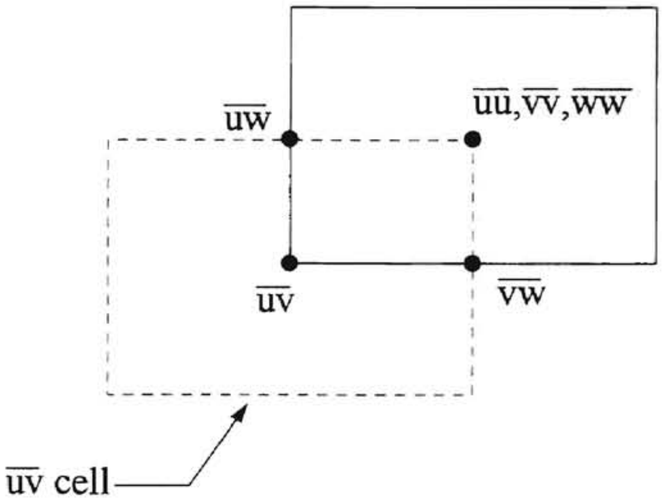

The staggered grid causes U and $\overline{uw}$ to be defined on all eastern and western boundaries; likewise, the V and $\overline{vw}$ on all southern and northern boundaries. The $\overline{uv}$ stress is defined on all boundaries. W, $\overline{u^2}$, $\overline{v^2}$, $\overline{w^2}$, and $\varepsilon$ are not defined on any boundaries and therefore must be interpolated.

## 2.4 Stability Enhancing techniques

The stability of the solution is maintained by three different methods in combination.

### 2.4.1 Apparent viscosity

The stress transport equations can be re-arranged so that each stress is equal to a quantity (called apparent viscosity) times the mean strain plus an additional source term. This apparent viscosity is added to the laminar viscosity in the mean flow equations which increases the connection between the mean flow strain and the turbulent stresses. It improves the stability of the equations by increasing the magnitude of the diagonal terms in the solution matrix instead of having large source terms[11]. The stresses are represented in the following form:

$$-\overline{u^2} = \nu_{11} \frac{\partial U}{\partial x} - S_{U,11} \qquad (24a) \qquad -\overline{v^2} = \nu_{22} \frac{\partial V}{\partial r} - S_{U,22} \qquad (24d)$$

$$-\overline{uv} = \nu_{12} \frac{\partial U}{\partial r} - S_{U,12} \qquad (24b) \qquad -\overline{uw} = \nu_{31} \frac{\partial W}{\partial x} - S_{U,31} \qquad (24e)$$

$$-\overline{uv} = \nu_{21} \frac{\partial V}{\partial x} - S_{U,21} \qquad (24c) \qquad -\overline{vw} = \nu_{32} \frac{\partial W}{\partial r} - S_{U,32} \qquad (24f)$$

Table 2.5. Apparent viscosities and source terms

| | apparent viscosity | | additional source term* |
|---|---|---|---|
| $\nu_{11}$ | $\dfrac{(2-1.333\,c_2)\overline{u^2}}{a_{11,p}+c_1\dfrac{\varepsilon}{k}}$ | $S_{u,11}$ | $-\overline{u^2}-\nu_{11}\dfrac{\partial U}{\partial x}$ |
| $\nu_{22}$ | $\dfrac{(2-1.333\,c_2)\overline{v^2}}{a_{22,p}+c_1\dfrac{\varepsilon}{k}}$ | $S_{u,22}$ | $-\overline{v^2}-\nu_{11}\dfrac{\partial V}{\partial y}$ |
| $\nu_{12}$ | $\dfrac{(1-c_2)\overline{v^2}}{a_{12,p}+c_1\dfrac{\varepsilon}{k}}$ | $S_{u,12}$ | $-\overline{uv}-\nu_{12}\dfrac{\partial U}{\partial y}$ |
| $\nu_{21}$ | $\dfrac{(1-c_2)\overline{u^2}}{a_{21,p}+c_1\dfrac{\varepsilon}{k}}$ | $S_{u,21}$ | $-\overline{uv}-\nu_{21}\dfrac{\partial V}{\partial x}$ |
| $\nu_{31}$ | $\dfrac{(1-c_2)\overline{u^2}}{a_{31,p}+c_1\dfrac{\varepsilon}{k}}$ | $S_{u,31}$ | $-\overline{uw}-\nu_{21}\dfrac{\partial W}{\partial x}$ |
| $\nu_{32}$ | $\dfrac{(1-c_2)\overline{v^2}}{a_{32,p}+c_1\dfrac{\varepsilon}{k}}$ | $S_{u,32}$ | $-\overline{vw}-\nu_{32}\dfrac{\partial W}{\partial y}$ |

*Source terms shown represent remainder of terms from each individual transport equation

### 2.4.2 Staggered grid arrangement

Examination of Figure 2.5 shows that the normal stresses are at the nodal points of each control volume, but the shear stresses are located on the borders. This has two benefits. First, when the stresses are calculated at these locations they can be directly substituted into the momentum equations without being interpolated (i.e. $\nu_{12}$ is needed on the south and north U control volume faces and $\nu_{11}$ is needed on the east and west U control volume faces, see Figure 2.5). Second, this arrangement relates the stresses and their major strains more directly. With the shear stress $\overline{uv}$ defined between both the U and V velocity grid points (see Figure 2.6 ) it adjusts immediately to changes in the velocity gradient. If during the iteration sequence a large gradient is generated between $U_N$ and $U_S$ the value of $\overline{uv}$ increases immediately. Since the $\overline{uv}$ stress appears explicitly in the U momentum equation it would result in a decrease in the velocity gradient. If the $\overline{uv}$ stress was not located between the velocity grid points it would not "feel" the entire effect of an increase in velocity gradient as quickly because the calculation of the gradient would involve interpolation[11].

Figure 2.5. Location of apparent viscosity in relation to mean velocity control volume

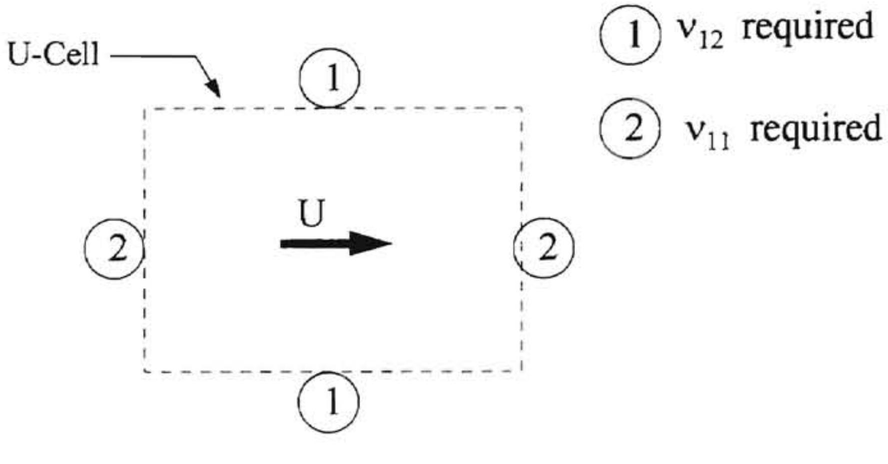

Figure 2.6. Location of velocities relative to shear stress

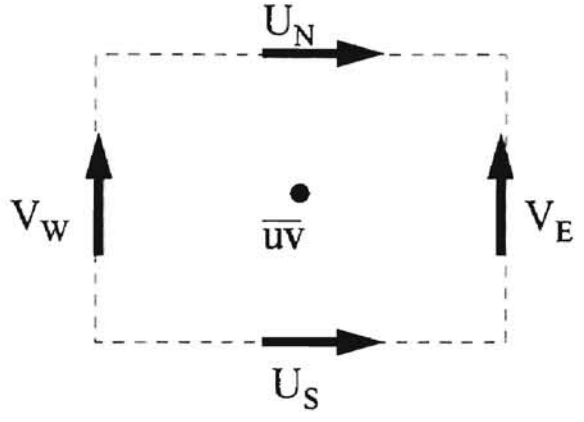

### 2.4.3 Positive normal stresses

As can be seen in (24), the apparent viscosities have the same sign as the normal stresses. Besides being physically impossible, a negative apparent viscosity during the iteration process would cause the solution to diverge. The positive value is maintained by ensuring that the $S_u$ term is always positive and the $S_p$ term is always negative for the normal stress equations. This is accomplished with the following algorithm:

$S_{u,\phi} = \max(S_u \text{ terms},0) + \min(S_p \text{ terms},0)/\phi$

$S_{p,\phi}=\max(S_p \text{ terms},0) + \min(S_u \text{ terms},0)\phi$

where max(a,b) returns the maximum value of a and b, likewise min(a,b) returns the minimum of a and b.

## 2.5 Boundary Conditions

### 2.5.1 Inlet

The inlet boundary conditions for U,V,W, $\overline{u^2}$, $\overline{v^2}$, $\overline{w^2}$, $\overline{uv}$, $\overline{uw}$, and $\overline{vw}$ are provided by the experimental data. A simple linear interpolation is used to calculate the values at the required gridpoint locations. However, with 20 uniform grid points in the radial direction, there is one grid point next to the north wall and two on the southern wall that must be extrapolated due to the coarseness of the experimental data. In the case of the U velocity, these three points are further adjusted so the volumetric flow rate agrees with the experimental data.

The turbulence dissipation is calculated from the given turbulence quantities. The following equation for dissipation is used[26]:

$$\varepsilon_{\text{inlet}} = \frac{k^{1.5}}{\lambda w} \qquad (25)$$

where $\lambda$=0.005 and w=width of the inlet.

The pressure fluctuation value is set equal to zero at the inlet boundary[29].

### 2.5.2 Walls

The above mentioned turbulence model is only valid for high Reynolds numbers[11,19]. In the area close to a wall (both stationary and moving) viscous effects become more important. Therefore, the turbulence models have to be modified to take this into account. To accurately model the flow near the wall, a large number of grid points would be required which would consume both computational memory and time. The best alternative to this is to use a function that adequately predicts the wall effects. The most common of these is the Launder and Spaulding Law of the Wall[38].

The law of the wall is essentially a logarithmic representation of the velocity profile parallel to the wall. The velocity at the node point, P, is determined by the wall shear stress, $\tau_w$. The control volume adjacent to the wall is divided into two sections, see Figure 2.7 below. The area from $r = 0$ to $r = r_v$ is the fully viscous sub-region where the turbulent shear stress is equal to zero. The area from $r = r_v$ to $r = \Delta$ is the fully turbulent region[11,26]. The thickness of the sublayer ($r_v$) is defined as

$$r_v = \frac{Re_v \, \mu}{\rho\sqrt{k}} \tag{26}$$

where $Re_v$ is a constant, set equal to 20. The non-dimensional form is

$$r_v^+ = \frac{\rho k^{\frac{1}{2}} C_\mu^{\frac{1}{4}} \Delta_P}{\mu} \tag{27}$$

Note: $r_v^+ = 11$ when $\Delta_P = r_v$.

For $r_v^+ < 11$, the grid point is inside the sublayer and the mean velocity parallel to the wall is defined as:

$$U_p = \frac{\tau_w}{\mu} \Delta_p \tag{28}$$

Figure 2.7. Grid point inside the viscous sublayer

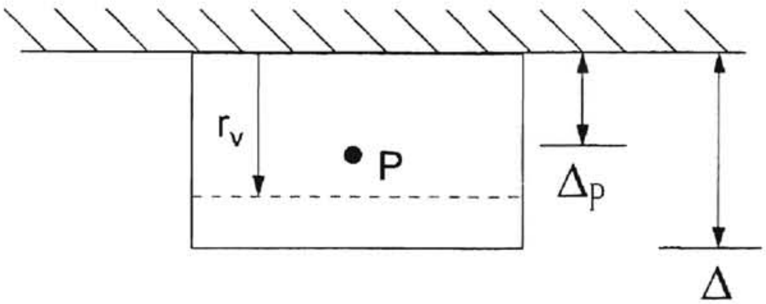

For $r_v^+ > 11$, the gridpoint is outside the sublayer and the mean velocity parallel to the wall is assumed to vary with distance from the wall according to:

$$\frac{U_P}{\sqrt{\frac{\tau_w}{\rho}}} = \frac{1}{\kappa}\ln\left(\frac{E\Delta_P\sqrt{\frac{\tau_w}{\rho}}}{\nu}\right) \tag{29}$$

In local equilibrium, where

$$k_P = \frac{\tau_w}{\rho\sqrt{c_\mu}}, \tag{29a}$$

the velocity at the node point P can be expressed in the following form:

$$\frac{U_P}{\frac{\tau_w}{\rho}} c_\mu^{0.25} k_P^{0.5} = \frac{1}{\kappa}\ln\left(\frac{Ey_P c_\mu^{0.25} k_P^{0.5}}{\nu}\right) \tag{30}$$

E and $\kappa$ are constants defined as 9.7 and 0.42 respectively. This gives an explicit equation for $\tau_w$ that can be used to approximate the viscous shear on the northern face of the control volume[11,26].

Figure 2.8. Gridpoint outside the viscous sublayer

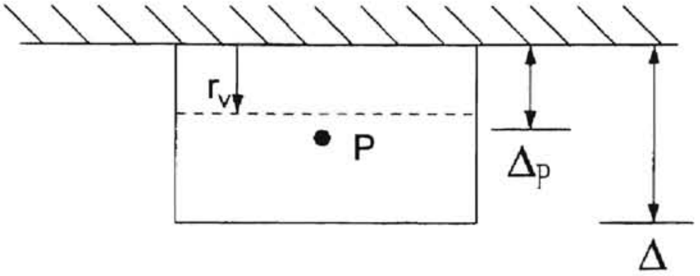

The W momentum equation is modified in the same manner as above, with $W_P$ and $\tau_{zr,w}$ substituted for $U_P$ and $\tau_w$ respectively, in the above equations.

The value of the wall shear stress calculated above is also used for the axial-radial turbulent shear stress, where

$$\overline{uv}_w = -\frac{\tau_{xr,w}}{\rho} \tag{31}$$

This is not physically correct because on the wall surface, the turbulent stress is actually zero. However, when the viscous sub-layer is very thin (as in this case), the gradient of $\overline{uv}$ across the control volume is represented very well by this approximation[11]. Note, (31) is for the northern wall, see Figure 2.9. The wall shear stress on the northern and southern walls have the same sign since the wall shear stress has the opposite sign of the velocity adjacent to the wall. The boundary condition for the southern wall has a sign change because the U velocity gradient has a change in sign but the shear stress must always be opposite the velocity vector, see Figure 2.10.

Figure 2.9. Axial-radial Reynolds shear stress b.c. on northern wall

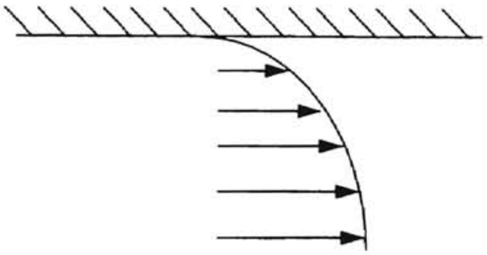

$$\frac{\partial U}{\partial r} < 0$$

$$\tau_{wall} < 0$$

$$\overline{uv}_w = -\frac{\tau_{wall}}{\rho} = \nu_{wall}\frac{\partial U}{\partial r}$$

Figure 2.10. Axial velocity profile on southern wall

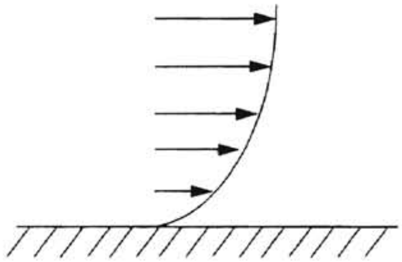

$$\frac{\partial U}{\partial r} > 0$$

$$\tau_{wall} < 0$$

$$\overline{uv}_w = \frac{\tau_{wall}}{\rho} = \nu_{wall}\frac{\partial U}{\partial r}$$

Likewise, the radial-azimuthal wall shear stress, $\tau_{zr,w}$, provides the boundary condition for the azimuthal-radial turbulent shear stress,

$$\overline{vw}_w = \frac{\tau_{zr,w}}{\rho} \qquad (32)$$

Note, unlike the $\overline{uv}$ boundary condition, there is no sign change for the $\overline{vw}$ boundary condition because there is no change in the W velocity gradient from northern to southern boundaries.

The axial-azimuthal shear stress, $\overline{uw}$ is set equal to zero at the wall since the main production term, $\overline{w^2}\frac{\partial W}{\partial x}$, is very small near the wall.

The normal turbulent stresses are calculated at the gridpoints adjacent to the wall with the following modifications:

- The values of the wall shear stress divided by density are substituted for the turbulent shear stresses in the production terms.
- The $\frac{\partial U}{\partial r}$ and $\frac{\partial W}{\partial r}$ terms that appear in the production terms are not approximated by their normal finite difference representation. Since the values of U and W are equal to zero along the northern boundaries, the normal gradients are represented by (see Figure 2.11 below):

$$\frac{\partial U}{\partial r} = \frac{-U_S}{\Delta} \qquad\qquad \frac{\partial W}{\partial r} = \frac{-W_S}{\Delta}$$

Figure 2.11. Approximation of velocity gradients normal to wall

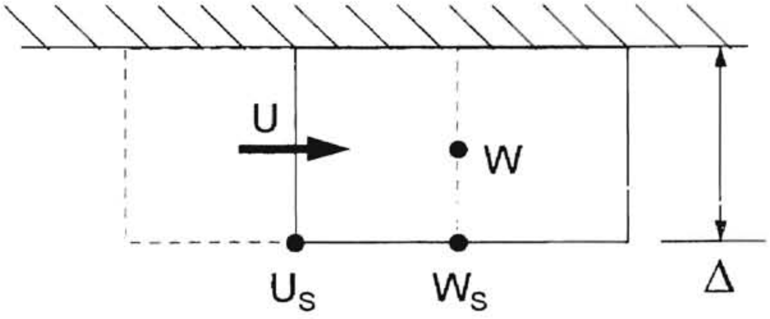

- The value of ε used in the turbulent transport equations at the wall is determined by the following equations[29]:

$$r_v^+ > 11 \qquad \varepsilon = \frac{c_\mu^{0.25}\sqrt{k_P}\,\ln(y^+)}{\kappa\Delta_P} \tag{33}$$

$$r_v^+ < 11 \qquad \varepsilon = \frac{c_\mu^{0.25}\sqrt{k_P}\,y^+}{\Delta_P} \tag{34}$$

- Turbulent diffusion is set equal to zero at the wall.

The boundary condition for the dissipation equation is forced instead of being calculated by the dissipation equation. This imposed value is shown below. Note, this is the value of $\varepsilon_p$ (i.e. the value of $\varepsilon$ at the gridpoint closest to the wall) not $\varepsilon_{wall}$.

$$\varepsilon_P = \frac{\left(\frac{\tau_w}{\rho}\right)^{1.5}}{\kappa\Delta_P} \tag{35}$$

Figure 2.12. Definition of dissipation on boundaries

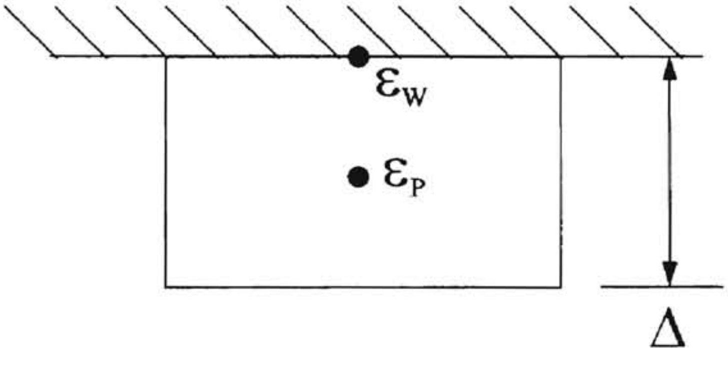

The methods described above apply for both stationary and rotating boundaries with the following modifications for the rotating boundary:

1. The $W_P$ velocity parallel to the wall in the log-law equation, (30) is the <u>relative</u> velocity with respect to the rotating boundary.

2. $\frac{1}{2}(\overline{v^2}+\overline{w^2})$ is used for the value of $k_P$ in (29a), instead of $\frac{1}{2}*(\overline{u^2}+\overline{v^2}+\overline{w^2})$. This modification is based on the assumption that $\overline{u^2}$ does not contribute very much to the radial-azimuthal wall shear stress, $\tau_{zr}$ This is based on the assumption that close to the wall convection and diffusion of turbulence kinetic energy is negligible, which allows the following assumption:

$$\tau_{wall} = \sqrt{\tau_{xr}^2 + \tau_{zr}^2} = (C_D C_\mu)\rho k$$

where $C_D$ and $C_\mu$ are constants equal to 1.0 and 0.09 respectively.

### 2.5.5 Outlet

The outlet boundary condition for the V, PP, $\overline{u^2}$, $\overline{v^2}$, $\overline{uv}$, and $\varepsilon$ equations is a zero gradient in the axial direction (i.e. $\frac{\partial}{\partial x}=0$). Since the swirl velocity profile across the annulus is constantly growing with increasing axial distance, the W, $\overline{w^2}$, $\overline{uw}$, and $\overline{vw}$ transport equations have a constant axial gradient at the boundary (see Figure 2.13 below).

Figure 2.13. Exit gradient boundary condition for swirl terms

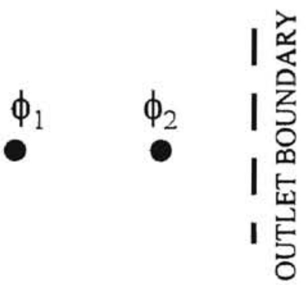

$$\frac{\partial \varphi_1}{\partial x} = \frac{\partial \varphi_2}{\partial x}$$

The outlet boundary condition for the U momentum equation involves taking the upstream value and adjusting it so that the exit volume flow equals the total inlet volume flow. A detailed description of the outlet U velocity boundary condition is given by Lilley[26].

### 2.6 Under-relaxation

Under-relaxation is used to reduce the size of oscillations of the calculated values during the iteration process. This is required due to the non-linear characteristics of the equations which may cause large oscillations or even divergence if not dampened. Two methods are used to under-relax the different variables.

The first method is to simply reduce the change between the new calculated value and the old value by a percentage (usually 30 to 50%). The equation representing this adjustment is shown below:

$$\phi_{new} = f_\phi \phi_{calculated} + (1 - f_\phi)\phi_{old} \qquad (36)$$

Typical values of (f) are 0.7 and 0.5 for 30% and 50% reduction respectively. This can be done implicitly without having to store the $\phi_{calculated}$ values with the following equation:

$$\frac{a_P}{f_\phi}\phi_P^{new} = a_N\,\phi_N + a_S\,\phi_S + a_E\,\phi_E + a_W\,\phi_W + S_U + \frac{(1-f_\phi)}{f_\phi}a_P\,\phi_P{}^{old} \qquad (37)$$

The second method of under-relaxation is commonly called the "inertia method." This method relaxes each individual cell differently based upon the mass unbalance of the cell. Cells that have a large mass unbalance are relaxed more than cells that have little mass unbalance. This allows the cells that are "well-behaved" to converge quickly and slows down the oscillations of the more active cells. This method is accomplished by modifying (37) as shown below, where M is the mass unbalance of the individual cell and c is a constant[11,26].

$$a_E\phi_E + a_W\phi_W + a_N\phi_N + a_S\phi_S + S_U + cM\phi_P{}^{old} = (a_P + cM)\phi_P \qquad (38)$$

Values of c and M are given below in Table 2.6, as suggested by Huang[11] and Lilley[26].

Table 2.6. Under relaxation and inertia relaxation constants

| | U | V | W | P | $\overline{u^2}$ | $\overline{v^2}$ | $\overline{w^2}$ | $\overline{uv}$ | $\overline{uw}$ | $\overline{vw}$ | $\varepsilon$ |
|---|---|---|---|---|---|---|---|---|---|---|---|
| $f_\phi$ | 0.5 | 0.5 | 0.5 | 0.7 | 0.7 | 0.7 | 0.7 | 0.7 | 0.7 | 0.7 | 0.7 |
| $M_\phi$ | 5 | 5 | 5 | N/A | 0 | 0 | 0 | 0 | 0 | 0 | 0 |

## 2.7 Convergence criterion

The solution is considered converged when the sum of the normalized residuals for each variable as well as the mass residuals for the pressure fluctuation equation are less than 0.009. The residuals for all of the individual variables ($\phi$) and mass are defined as:

$$\mathrm{resor}_{\phi} = \frac{\Sigma_{i,j=1,1,ni,nj} \left| \Sigma a_i \phi_i + Su - a_P \phi_P \right|}{Q_{in}\phi} \tag{39}$$

$$\mathrm{resor}_{mass} = \frac{\Sigma_{i,j=1,1,ni,nj} \left| \text{mass unbalance} \right|}{Q_{in}\rho} \tag{40}$$

## 2.8 Numerical Solver

The 11 partial differential equations are solved using an alternating direction Tridiagonal Matrix Algorithm (TDMA) numerical solver. The algorithm alternatingly walks in the axial direction sweeping in the radial direction, then walks in the radial direction and sweeps in the axial direction. The number of sweeps can be varied for each independent variable. Different numbers were experimented with but the best combination to minimize the of number of iterations and convergence time but maintain accuracy is given below in Table 2.7[11,29].

Table 2.7. Number of sweeps for each variable

| U | V | W | P | $\overline{u^2}$ | $\overline{v^2}$ | $\overline{w^2}$ | $\overline{uv}$ | $\overline{uw}$ | $\overline{vw}$ | $\varepsilon$ |
|---|---|---|---|---|---|---|---|---|---|---|
| 2 | 2 | 2 | 3 | 4 | 4 | 4 | 4 | 4 | 4 | 2 |

## 2.9 Flow diagram of code

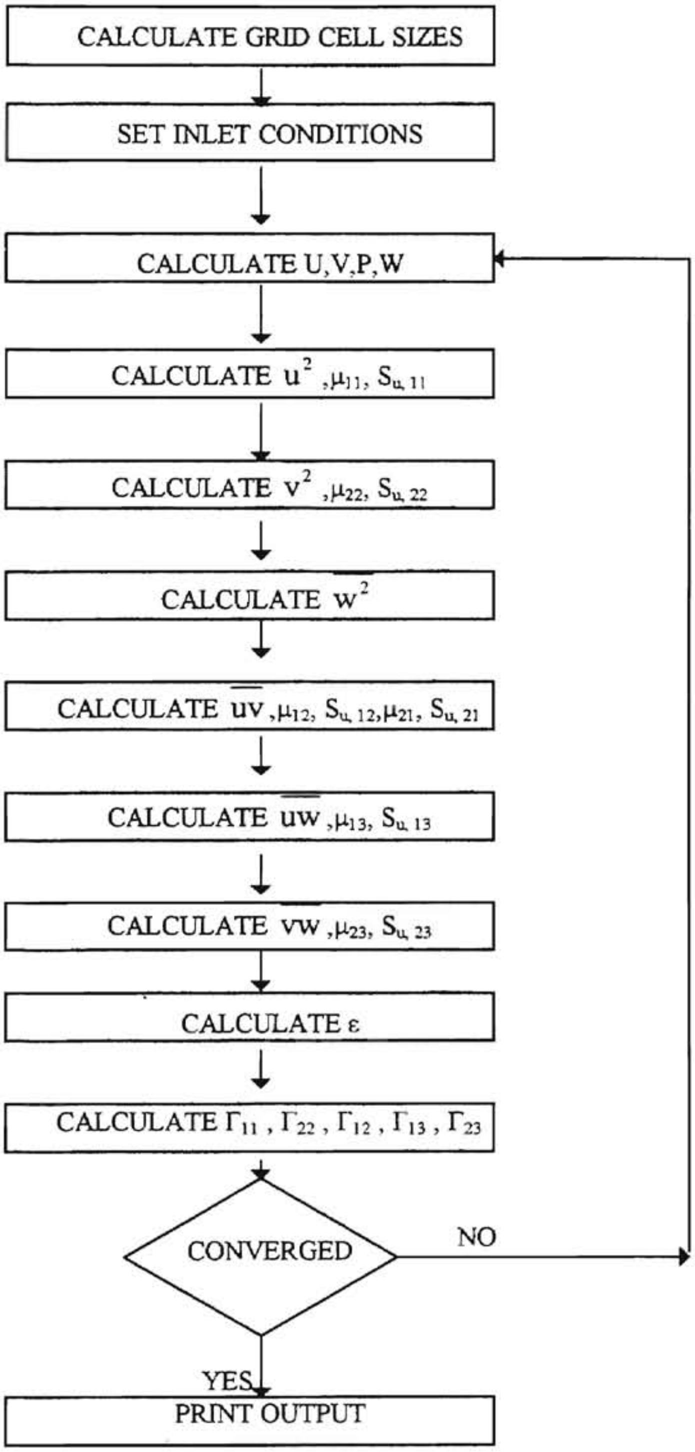

# CHAPTER III

# RESULTS AND DISCUSSION

## 3.1 Profiles of RSM results along seal length

Contour and profile plots along the length of the seal are shown for U,V,W, $\overline{u^2}$, $\overline{v^2}$, $\overline{w^2}$, $\overline{uv}$, $\overline{uw}$, and $\overline{vw}$ in Figures 3.1-3.18. The axial location is non-dimensionalized with the seal clearance(c). The radial location is displayed as a function of n/c, where n is the normal distance from the rotor surface, see Figure 3.0 below.

Figure 3.0. Computational geometry

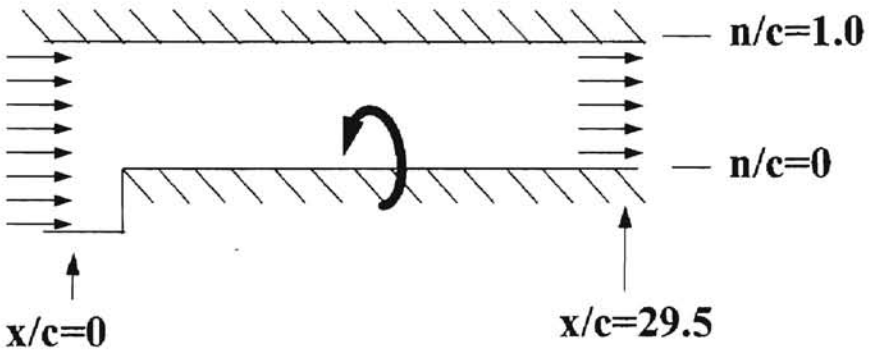

As can be seen in Figure 3.2, the axial velocity begins with an entrance region where the centerline velocity is approximately 15 percent larger than the average. By x/c=29.5, the axial velocity profile is approaching the fully developed flow. The mean radial velocity (V) is negligible except immediately adjacent to the forward facing step, see Figures 3.3 and 3.4. The flow could actually be approximated using only U and W if the results were taken at x/c > 10. The W velocity profiles show how the momentum from the rotating inner annulus is being transferred to the fluid as the axial distance increases, see Figure 3.5

and 3.6. Eventually we should expect the W velocity profile to approach Couette flow between the two cylinders.

As can be seen in Figure 3.7 and 3.8, the magnitude of the axial Reynolds normal stress($\overline{u^2}$) is greatest adjacent (but not immediately close) to the walls. The $\overline{u^2}$ values close to the rotating wall are approximately twice the value of those close to the stationary wall and continue to grow along the length of the seal. This is obviously caused by the transfer of turbulent kinetic energy from the azimuthal Reynolds normal stress which has a very large production term near the rotating wall. Likewise, values of $\overline{u^2}$ are lower in the centerline of the annulus where the mean strain terms are lower.

The radial Reynolds normal stress contours show that the magnitude of $\overline{v^2}$ is highest close to the rotating wall as well (Figures 3.9 and 3.10). All of this turbulence is produced by the rotating wall since the values of $\overline{v^2}$ are nearly zero at the inlet. The $\overline{v^2}$ values become quite low away from the rotating wall, this is to be expected since all of the terms in the $\overline{v^2}$ production equation are negligible except for the $\overline{vw}\frac{W}{r}$ term, see (23b). As will be seen below, the $\overline{vw}$ values are highest immediately close to the wall and of course the azimuthal velocity is greatest there as well. Likewise, diffusion of turbulence quantities close to the wall is very low.

The azimuthal Reynolds normal stress profiles are very similar to the radial normal stress profiles, just larger in magnitude (Figures 3.11 and 3.12). This is reasonable since the production terms are similar; however, the radial normal stresses are not dampened by the horizontal walls as much as the $\overline{v^2}$ values[10]. This can be seen in Figures 3.10 and 3.12 close to the rotating boundary. The $\overline{v^2}$ values decrease rapidly close to the wall, but the $\overline{w^2}$ values do not change dramatically.

The axial-radial Reynolds shear stress contours/profiles (Figures 3.13 and 3.14) demonstrate that $\overline{uv}$ is zero close to the center of the flow and has a sign change across the centerline. This is very reasonable since the largest production term for $\overline{uv}$ (see equation 23d) , $\overline{v^2}\frac{\partial U}{\partial r}$, changes sign across the flow as well[10,18]. Likewise, the values of $\overline{uv}$ are higher close to the rotating wall due to the swirl term, $\overline{uw}\frac{W}{r}$, as well as the fact that $\overline{v^2}$ is higher close to the rotating wall than the stationary wall.

As would be expected, the axial-azimuthal and radial-azimuthal Reynolds shear stresses (Figures 3.15,16,17, and 18) are largest close to the rotating wall. Likewise, these larger values spread across the flow area as the axial distance increases. The increasing magnitude of $\overline{uw}$ at the rotating wall is a direct result of the fact that the $\overline{uv}\frac{\partial W}{\partial r}$ term in its production equation is increasing along the wall as well. Likewise, the fact that the $\overline{vw}$ values decrease immediately close to the rotating wall is due to a decrease in its largest production term, $\overline{v^2}\frac{\partial W}{\partial r}$, because of the large decrease in $\overline{v^2}$ in the same area.

Figure 3.1. Axial velocity contours (m/s)

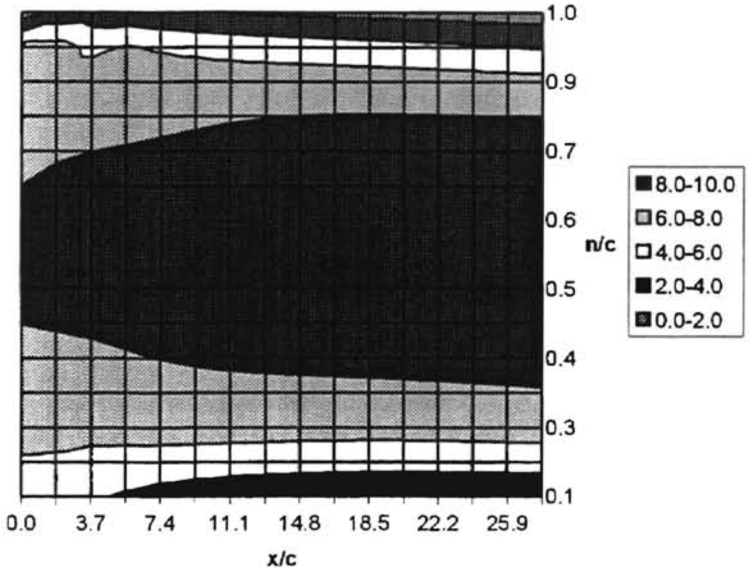

Figure 3.2. Axial Velocity profiles

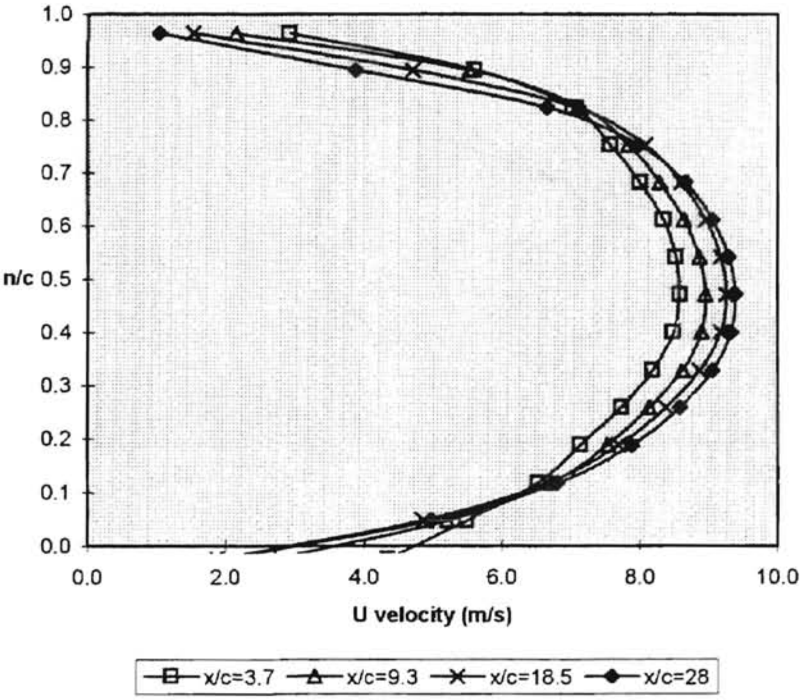

Figure 3.3. Radial Velocity Contours
(m/s)

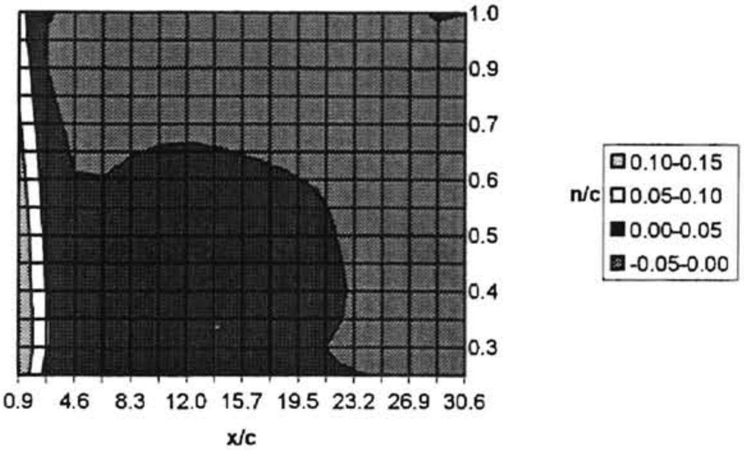

Figure 3.4. Radial Velocity Profiles

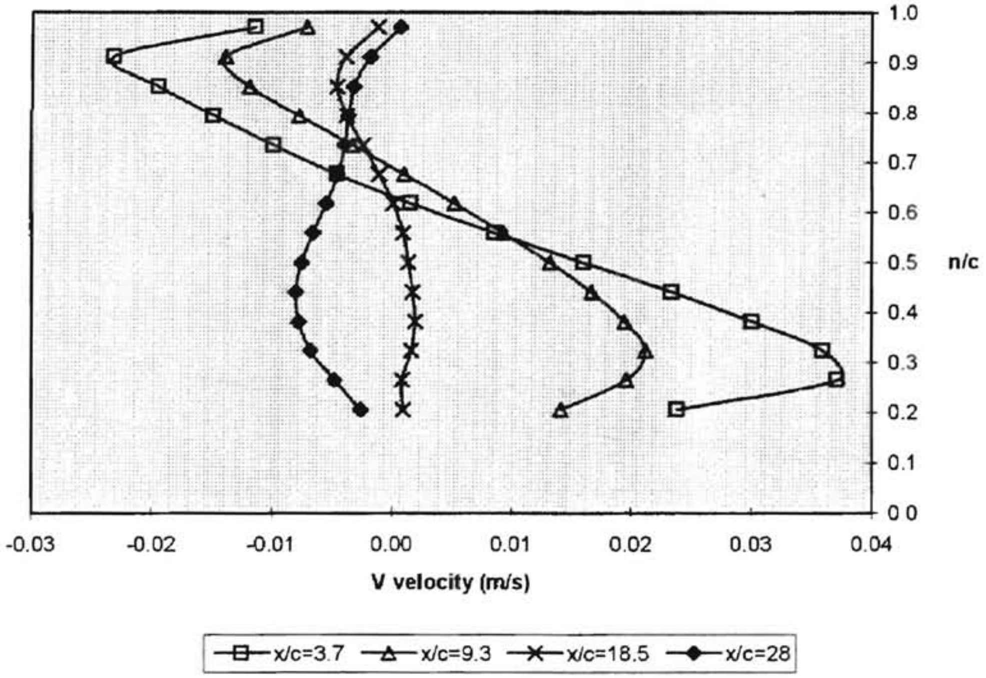

**Figure 3.5. Azimuthal velocity contours (m/s)**

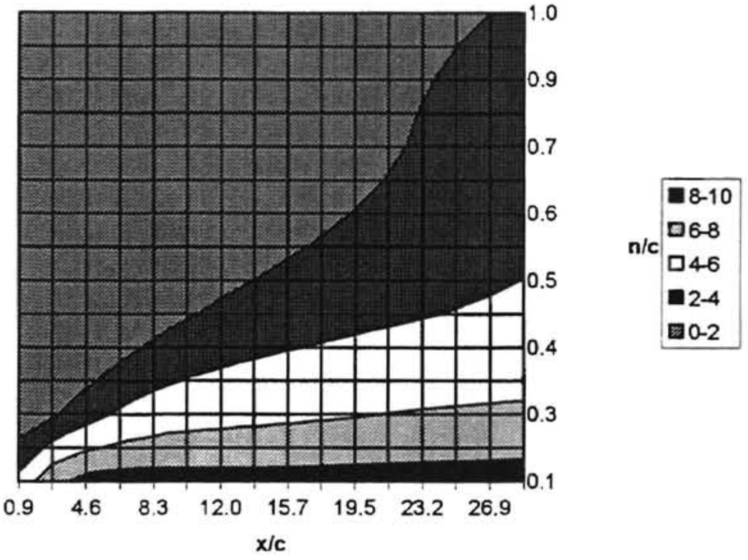

**Figure 3.6. Azimuthal Velocity Profiles**

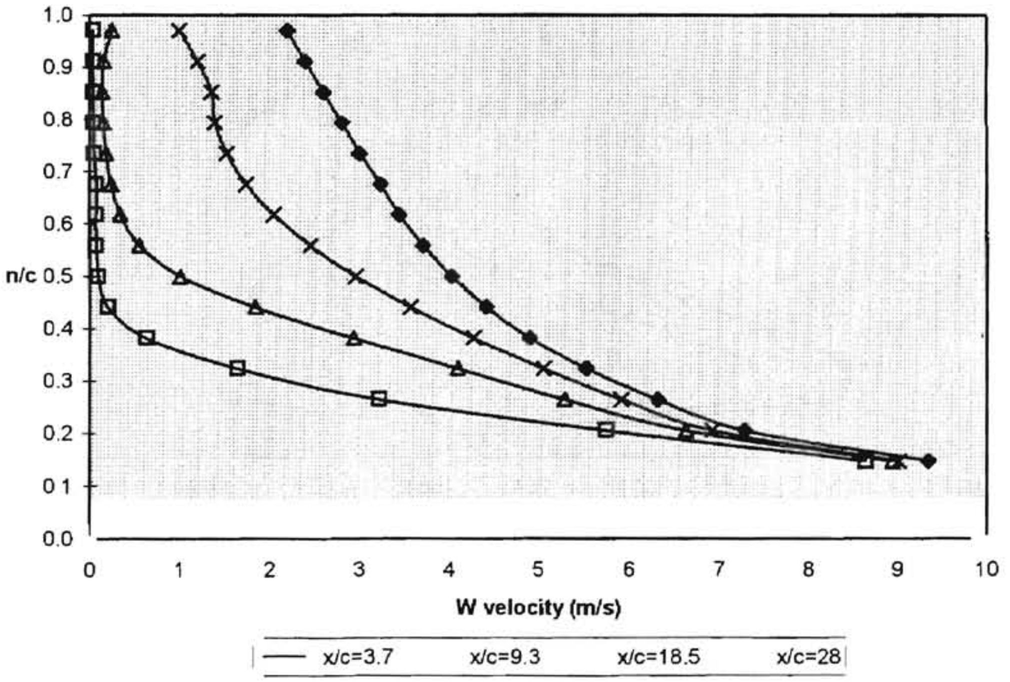

**Figure 3.7. Axial Reynolds normal stress contours ($m^2/s^2$)**

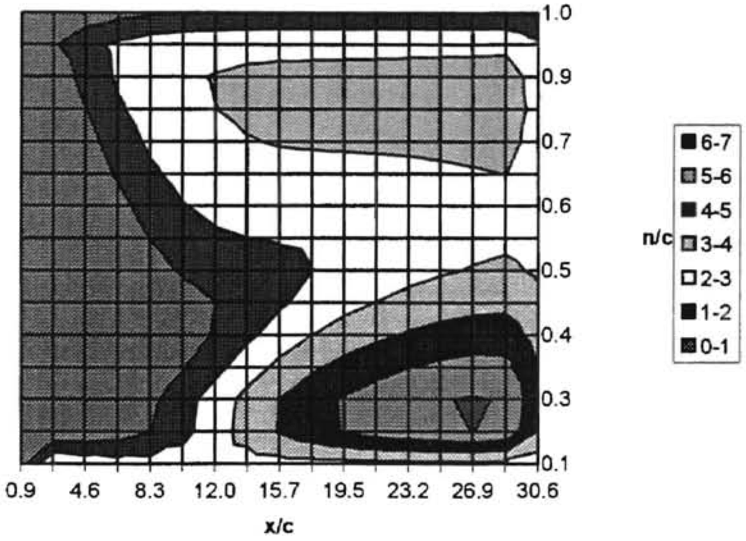

**Figure 3.8. Axial Reynolds normal stress profiles**

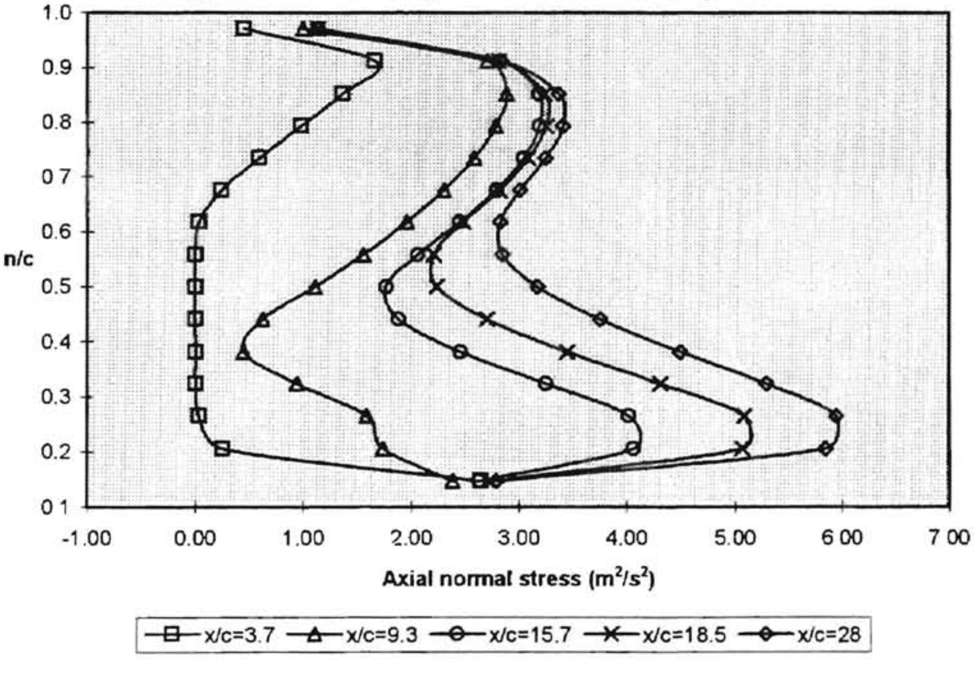

Figure 3.9. Radial Reynolds normal stress contours ($m^2/s^2$)

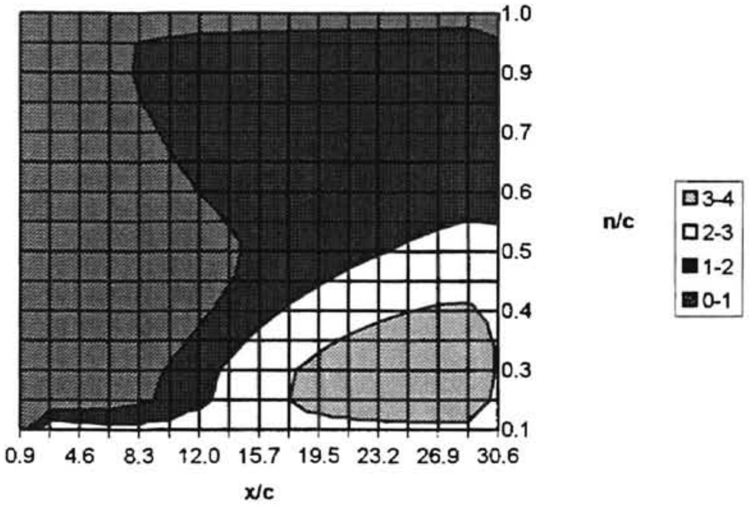

Figure 3.10. Radial Reynolds normal stress profiles

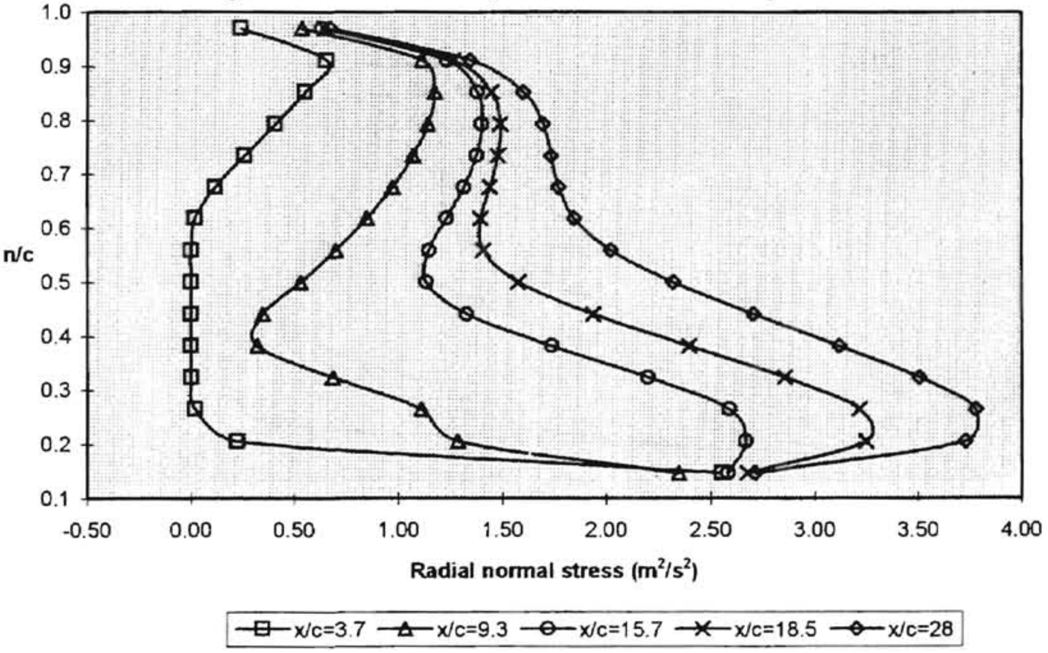

Figure 3.11. Azimuthal Reynolds normal stress contours ($m^2/s^2$)

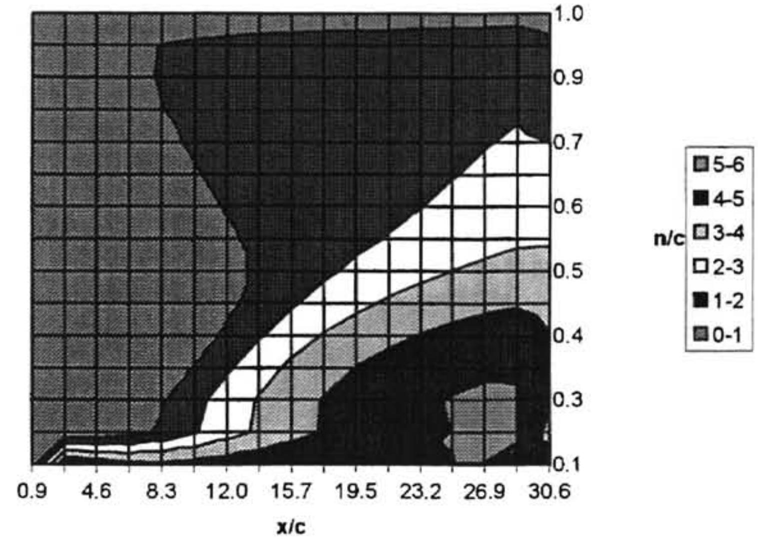

Figure 3.12. Azimuthal Reynolds normal stress profiles

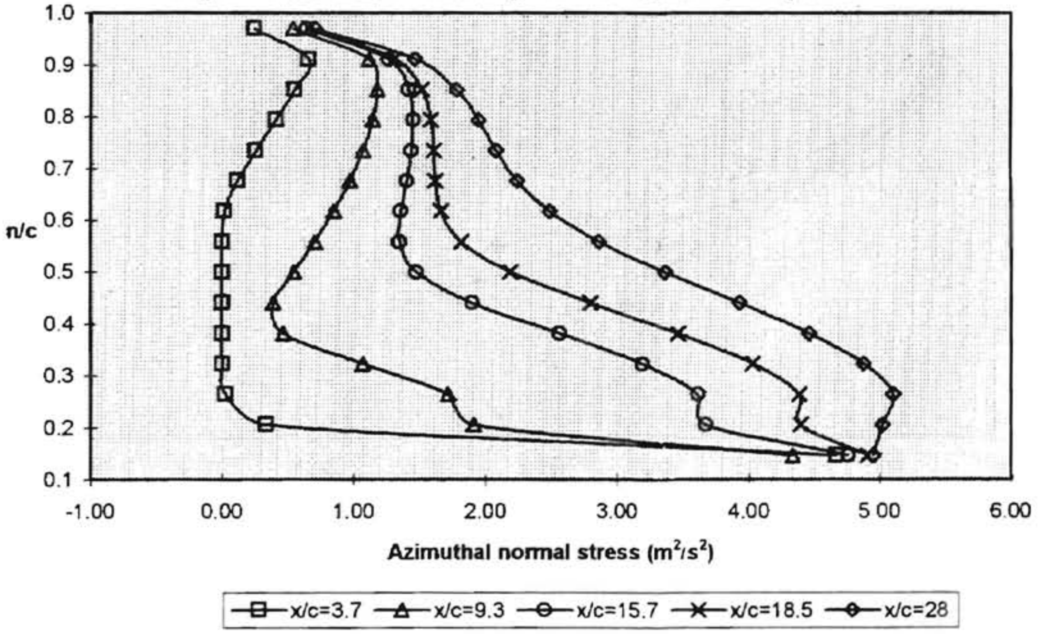

Figure 3.13. Axial-radial Reynolds shear stress contours ($m^2/s^2$)

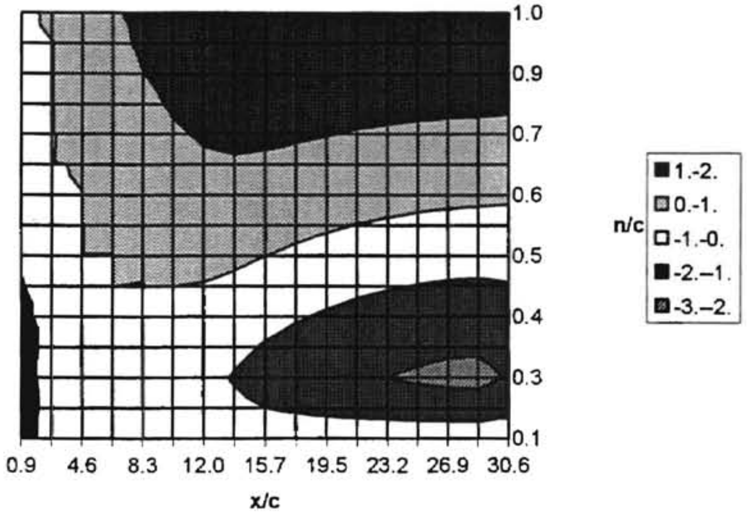

Figure 3.14. Axial-radial Reynolds shear stress profiles

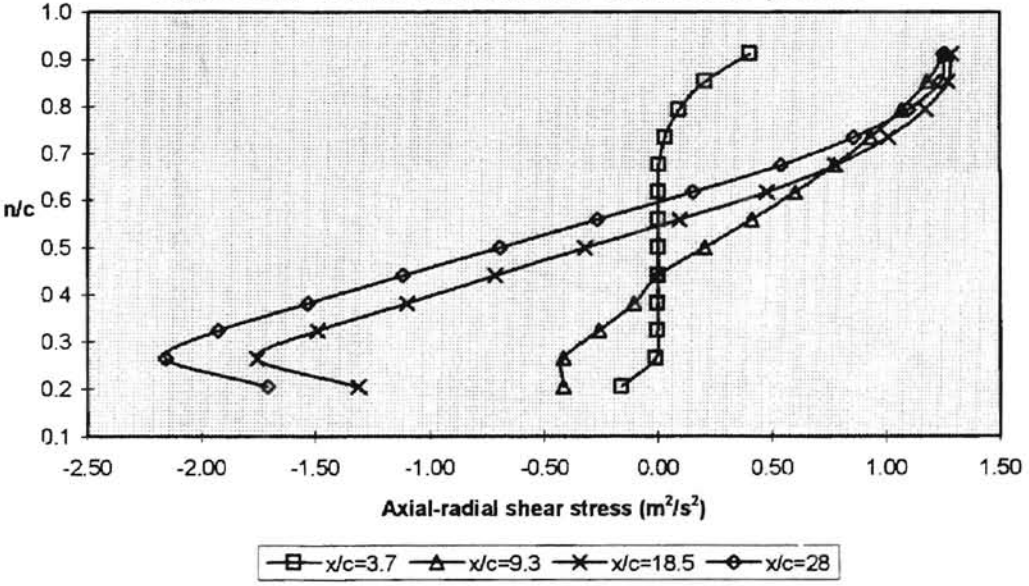

**Figure 3.15. Axial-azimuthal Reynolds shear stress contours ($m^2/s^2$)**

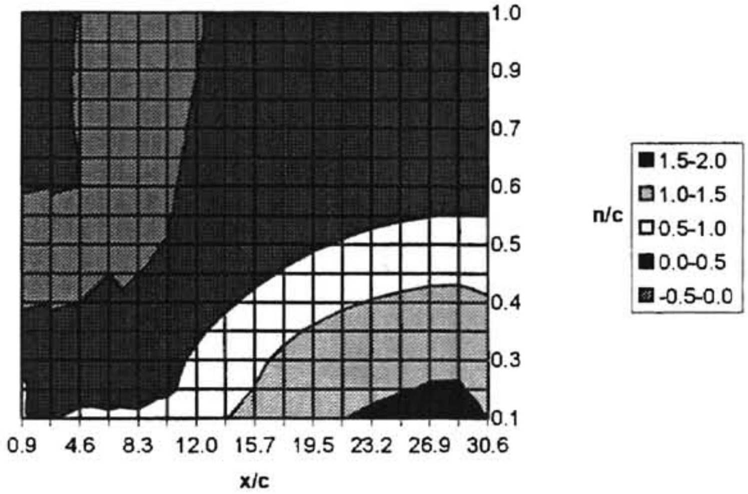

**Figure 3.16. Axial-azimuthal Reynolds shear stress profiles**

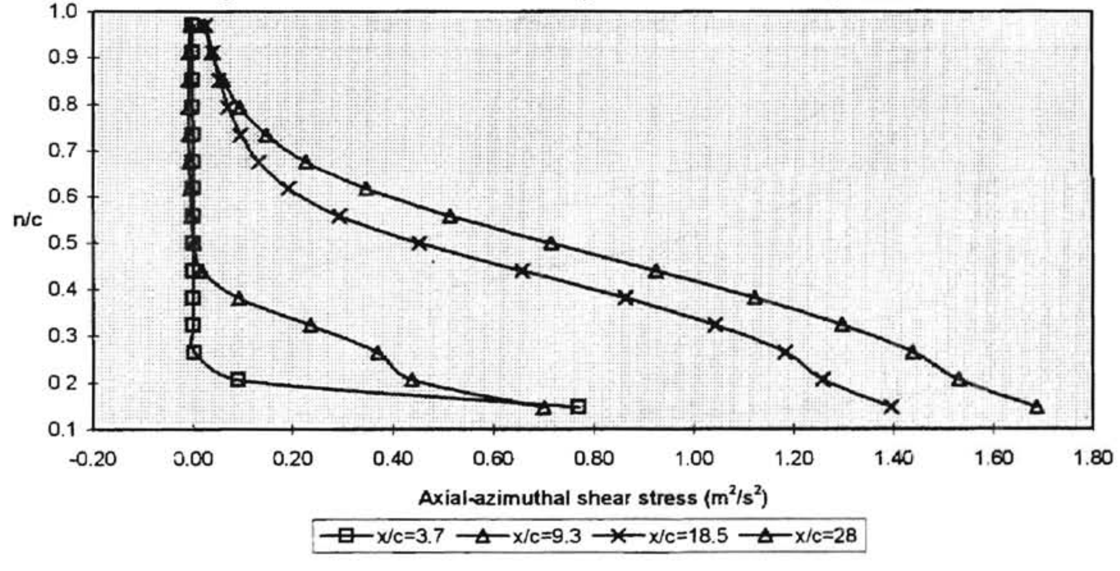

Figure 3.17. Radial-azimuthal Reynolds shear stress contours ($m^2/s^2$)

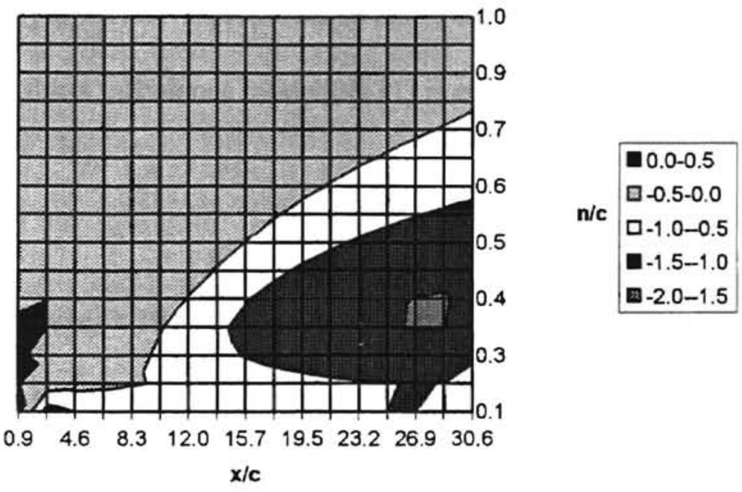

Figure 3.18. Radial-azimuthal Reynolds shear stress profiles

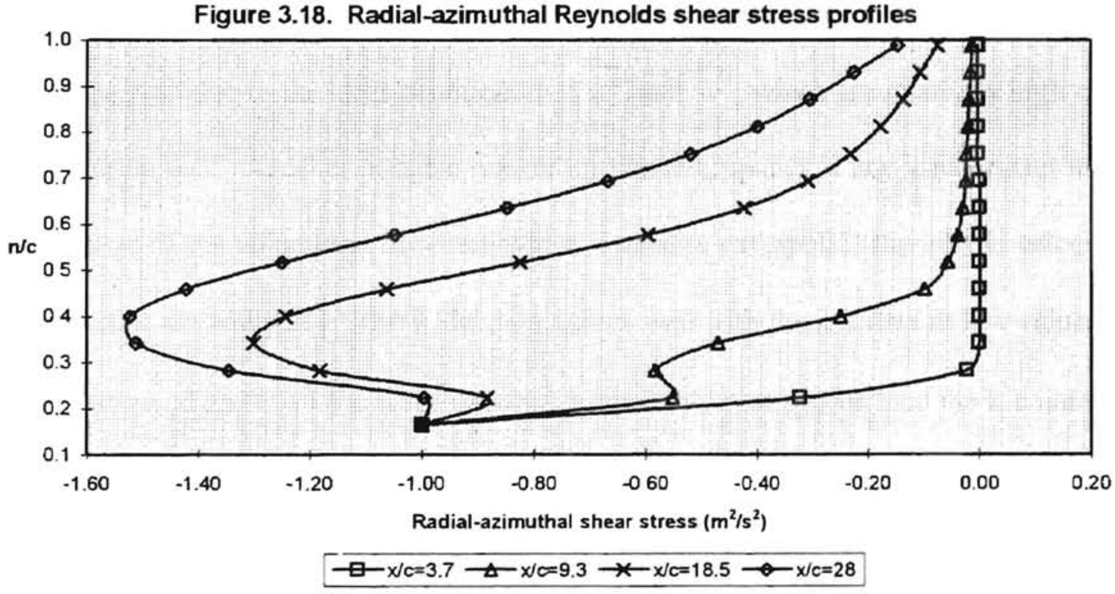

### 3.2 Comparison of computational and experimental data

Figures 3.19-3.34 compare the data from the RSM and the published experimental data of Morrison, et al. [27] at various axial positions along the seal. Additionally, mean velocity data from a standard k-ε turbulence model[26,31] is compared against the RSM data in Figures 3.19-3.24.

As can be seen in Figures 3.19-3.21 the RSM overpredicts the viscous drag of the walls. The profile is more accurate adjacent to the stationary wall. This may indicate that the method used to model the rotating wall is producing too much "apparent viscosity". This would mean that the $\mu_{12}$ term has a higher magnitude than necessary. Since $\mu_{12}$ is directly proportional to $\overline{v^2}$ and k this indicates that turbulence energy levels may be too high close to the wall due to the large production of $\overline{u^2}$ and $\overline{w^2}$ which are relatively high close to the rotating wall. Another possible reason for this discrepancy is any inaccuracies in measurement of the volumetric flow rate which is used to extrapolate the inlet U velocity values next to the walls[26]. The RSM data agrees well with the k-ε data at low values of x/c. However, at x/c=29.5 the RSM data has a much different profile than the k-ε data. This is a result of the isotropic nature of the k-ε model.

Figures 3.22-24 demonstrate the good agreement between the RSM, k-ε, and experimental mean azimuthal velocity profiles. As can be seen the W velocity profile predicted by RSM is less linear across the channel which may indicate that viscous effects have too dominant a role over convective components. As with the U velocity profiles seen above, this can be accounted for by large values of turbulence energy adjacent to the rotating wall.

The RSM does a poor job of predicting the azimuthal Reynolds normal stress at x/c=5 and x/c=13 (Figures 3.25 and 3.26), especially close to the rotating wall. The large "dip" in the $\overline{w^2}$ profiles generated by the RSM is a result of the azimuthal turbulence spreading upward from the rotating inner cylinder as the axial distance along the seal increases. Since the inlet values of $\overline{w^2}$ are quite low, it is interesting that at x/c=5 the experimental data shows that $\overline{w^2}$ has already spread across more than half the flow domain. Since the largest production term for $\overline{w^2}$ is $\overline{vw}\frac{\partial W}{\partial r}$, and the computed W profiles agree well with the experimental data, this indicates that the $\overline{vw}$ profile adjacent to the wall is not correct for x/c < 20. The RSM does a much better job of predicting the $\overline{w^2}$ values closer to the seal outlet (see Figure 3.27).

A comparison between the computational and experimental axial-radial Reynolds shear stress data for three axial positions is shown in Figures 3.28-30. The inflection point in the $\overline{uv}$ curves close to the rotaiting wall in Figures 3.29 and 3.30 is caused by the large values of $\overline{v^2}\frac{\partial U}{\partial r}$ at that location. These figures indicate that there may be an inconsistency in the experimental data because unlike the computational data, the experimental $\overline{uv}$ profiles do not pass through zero. The largest production term for $\overline{uv}$ in this particular flow is the $\overline{v^2}\frac{\partial U}{\partial r}$ term. Since the U velocity profile has an inflection point (i.e. goes through zero) close to the center of the channel, the $\overline{uv}$ should as well.

As can be seen in Figure 3.31 the computational and experimental data both show that the magnitude of $\overline{u^2}$ is higher close to the walls than in the center of the channel where the mean strain terms are lower. Overall, the RSM predicts higher values of $\overline{u^2}$ than are shown in the experimental data.

The RSM underpredicts the values of $\overline{v^2}$ in comparison to the experimental data, especially close to the rotating wall(Figure 3.32). The experimental values seem very large considering the fact that the values of the radial velocity are very low throughout the flow and the only production term in the $\overline{v^2}$ equation involving the azimuthal velocity is $\overline{vw}\frac{W}{r}$. It is also difficult to understand the value of $\overline{v^2}$ being so large close to a solid boundary where the radial velocity is zero.

The comparison between computational and experimental data for $\overline{uw}$ is shown in Figure 3.33 Overall the RSM overpredicts the value of $\overline{uw}$ in comparison to the experimental data but the profiles are very similar in shape and magnitude. The actual difference between the two sets of data is only about 1.5 $m^2/s^2$.

The radial-azimuthal profiles at x/c=29.5 are shown in Figure 3.34. The computational data is larger in magnitude close to the rotating wall because it is set equal to the wall shear stress term, $\tau_{32}/\rho$, at n/c=0. This value is quite large close to the rotating wall because the magnitude of $\frac{\partial W}{\partial r}$ (which is part of the largest production term for $\overline{vw}$) is very high in this region. The experimental data does not indicate the larger values of $\overline{vw}$ close to the rotating wall even though the experimental data does show that $\frac{\partial W}{\partial r}$ is very large in this area. As indicated above, this is a possible reason for the discrepancy in the $\overline{w^2}$ data.

Another possible reason for the discrepancy between the turbulence data predicted by the RSM and the published experimental data is the exclusion of the "wall reflection" terms from the current model[11,19]. These "wall reflection" terms account for the simultaneous influence of both x and r walls. This has the net effect of increasing the impact mean strain production terms have on all of the stresses, not just the principal stresses. For instance, the $\overline{u^2}$ transport equation would be effected by not only $P_{11}$, but by $P_{22}$ and $P_{33}$ terms as well. The addition of these wall reflection terms would improve the RSM's ability to predict the return to more isotropic flow at larger X/C values. This should cause the axial velocity profile predicted by the RSM to look more like the published experimental data.

Figure 3.19. Comparison of Axial velocity data at X/C=5

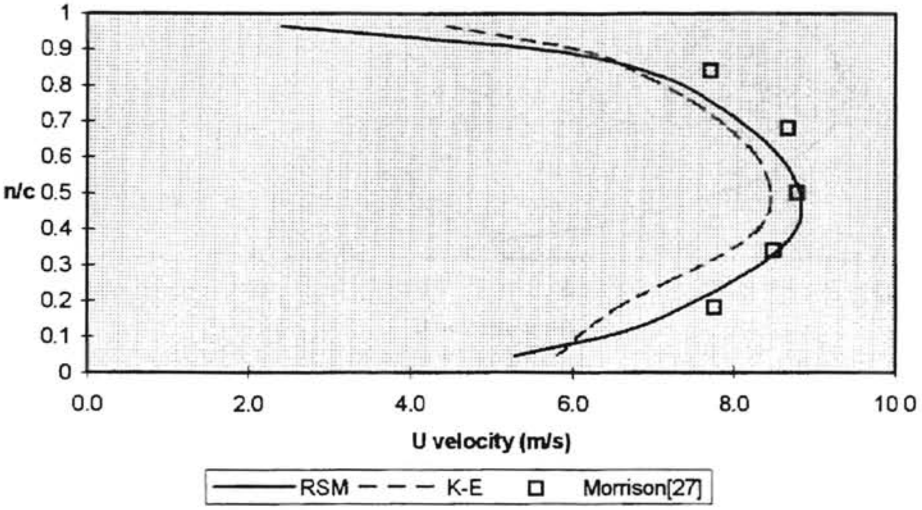

Figure 3.20. Comparison of Axial velocity data at at X/C=13

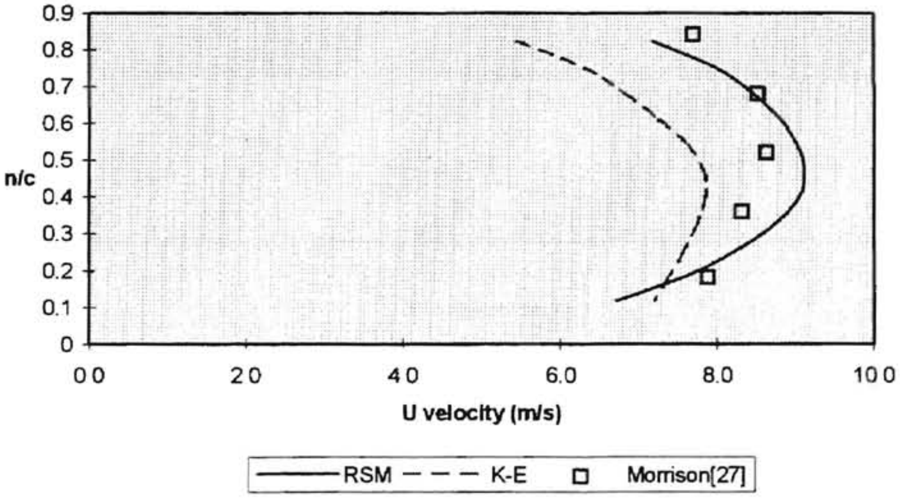

Figure 3.21. Comparison of Axial velocity data at X/C=29.5

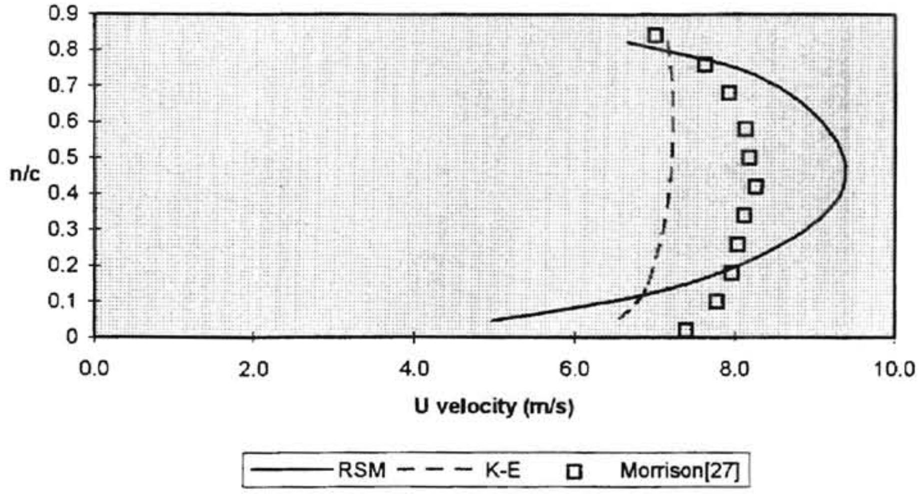

Figure 3.22. Comparison of Azimuthal velocity data at X/C=5

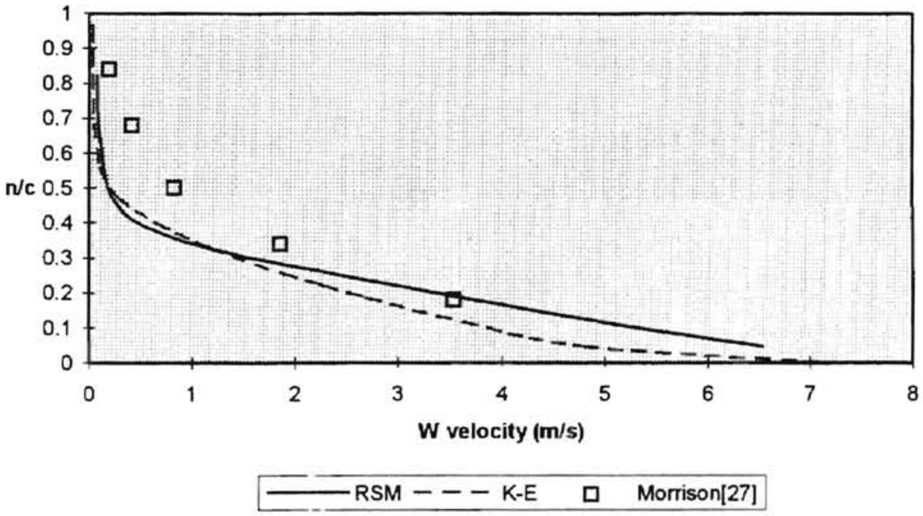

Figure 3.23. Comparison of Azimuthal velocity data at X/C=13

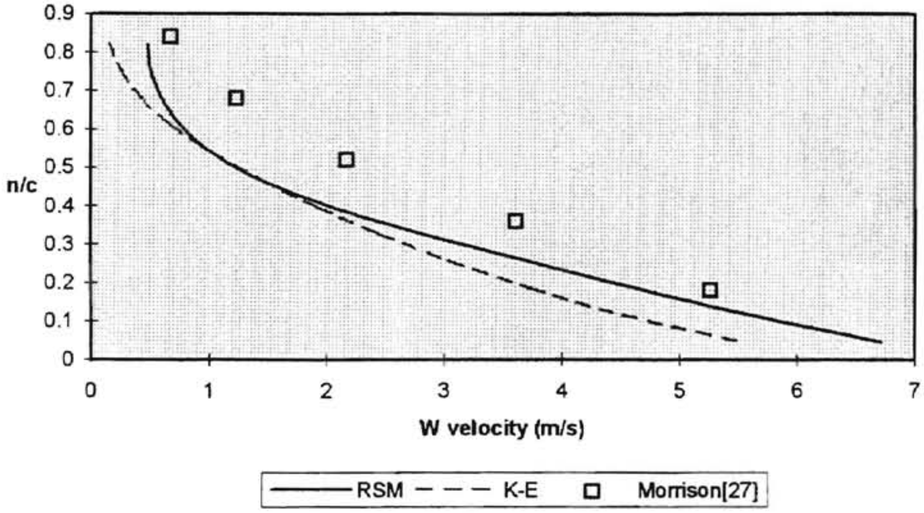

Figure 3.24. Comparison of Azimuthal velocity data at X/C=29.5

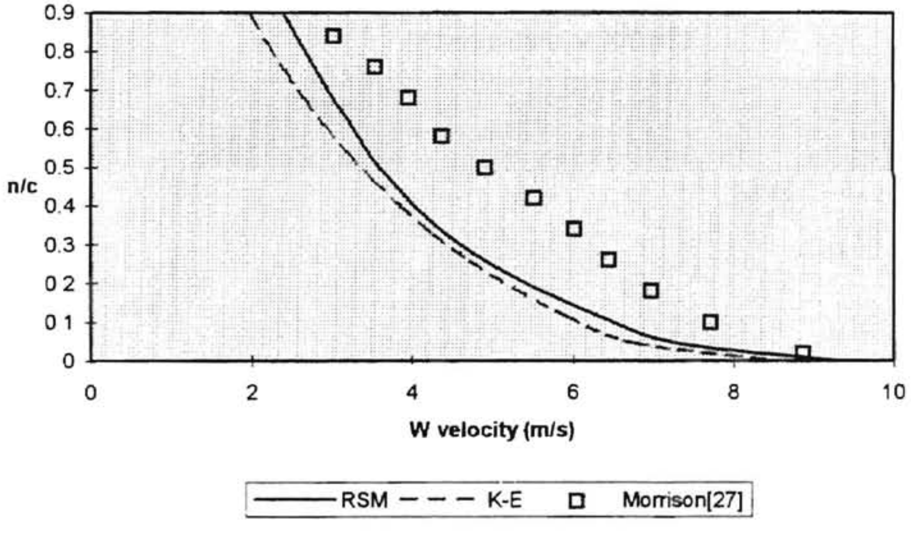

**Figure 3.25. Comparison of azimuthal Reynolds normal stress data at X/C=5**

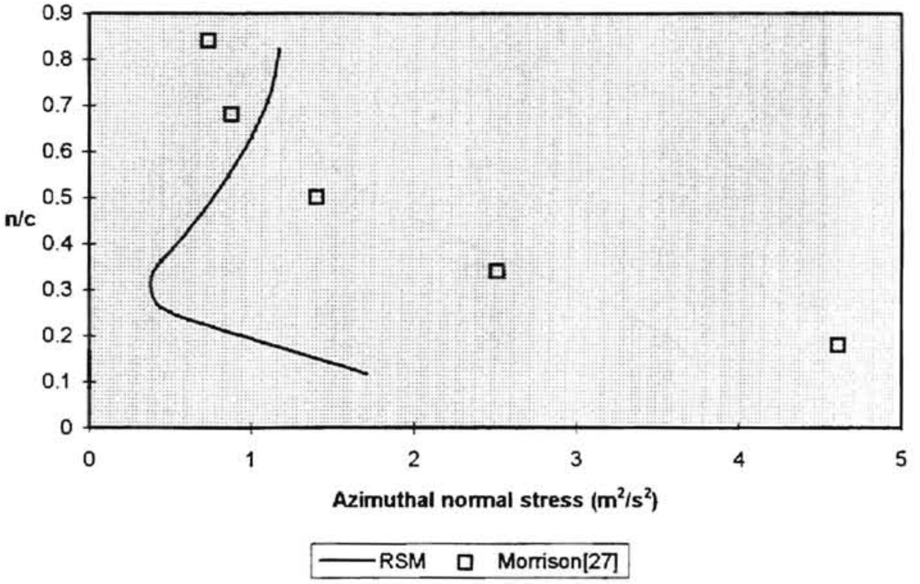

**Figure 3.26. Comparison of azimuthal Reynolds normal stress data at X/C=13**

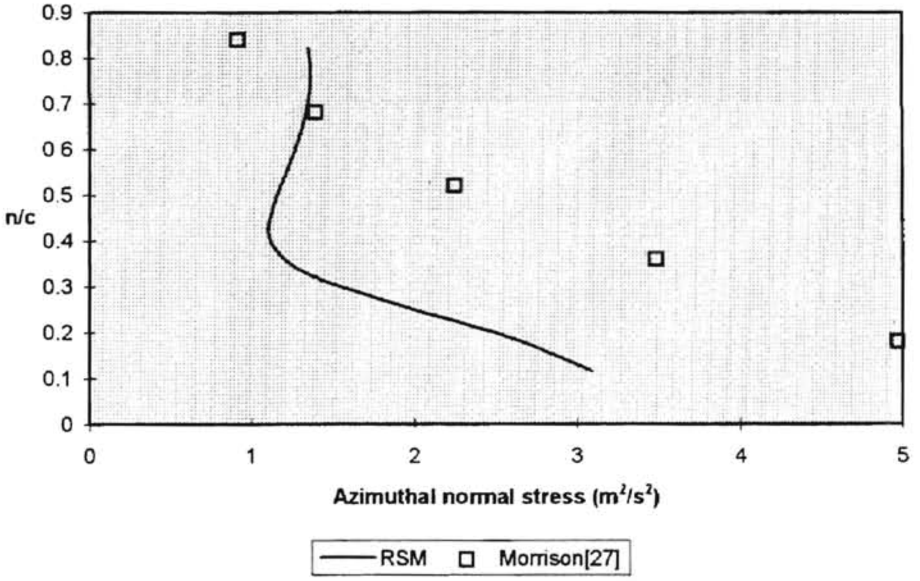

Figure 3.27. Comparison of azimuthal Reynolds normal stress data at X/C=29.5

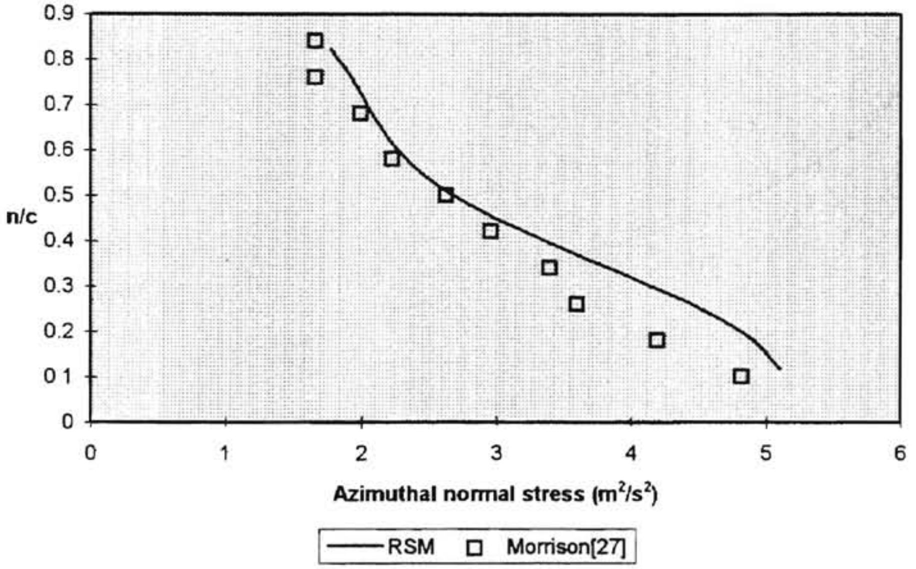

Figure 3.28. Comparison of axial-radial Reynolds shear stress data at X/C=5

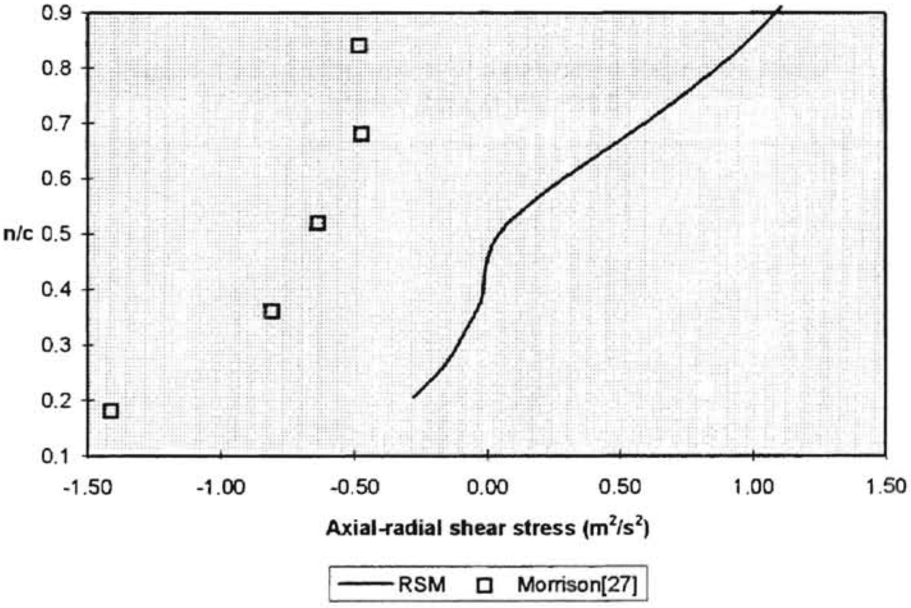

Figure 3.29. Comparison of axial-radial Reynolds shear stress data at X/C=13

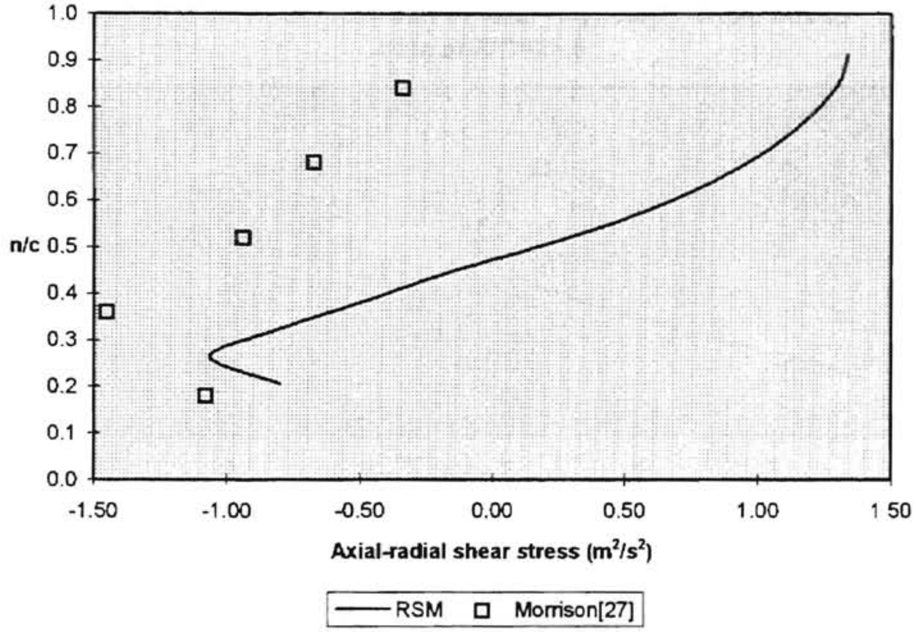

Figure 3.30. Comparison of axial-radial Reynolds shear stress data at X/C=29.5

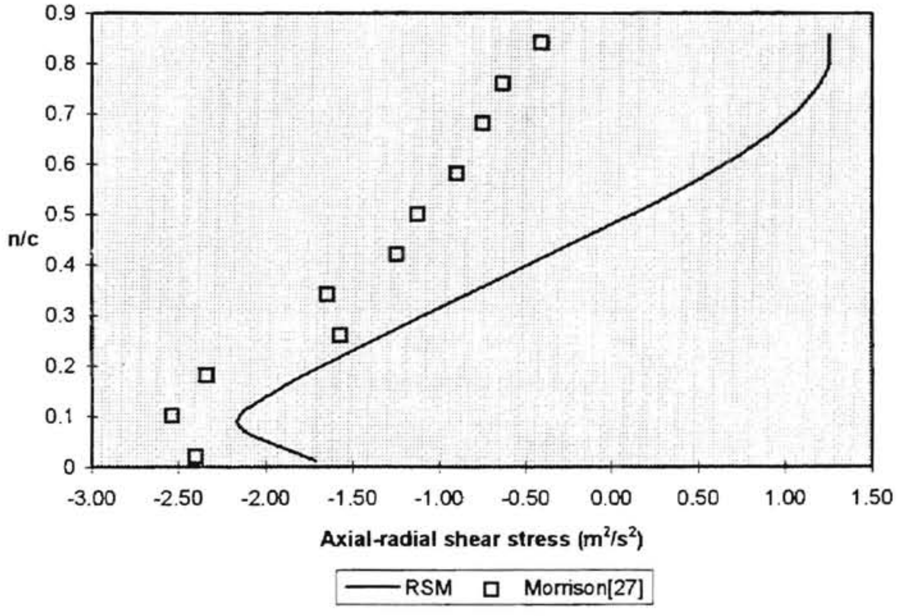

Figure 3.31. Comparison of axial Reynolds normal stress data at X/C=29.5

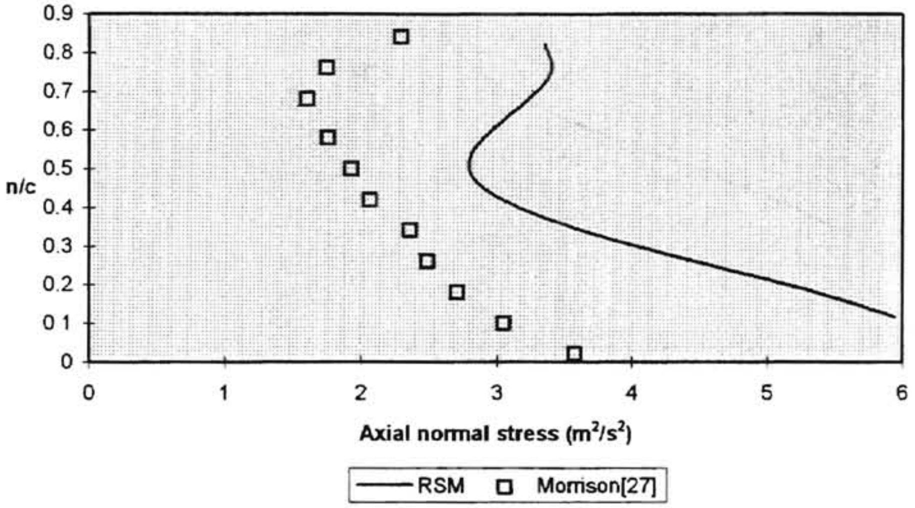

Figure 3.32. Comparison of radial Reynolds normal stress data X/C=29.5

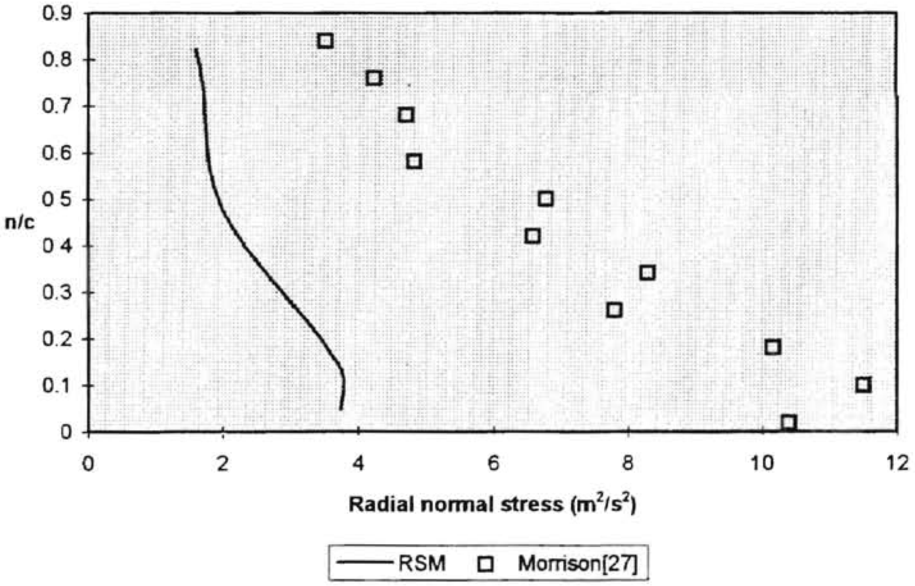

Figure 3.33. Comparison of axial-azimuthal Reynolds shear stress data at X/C=29.5

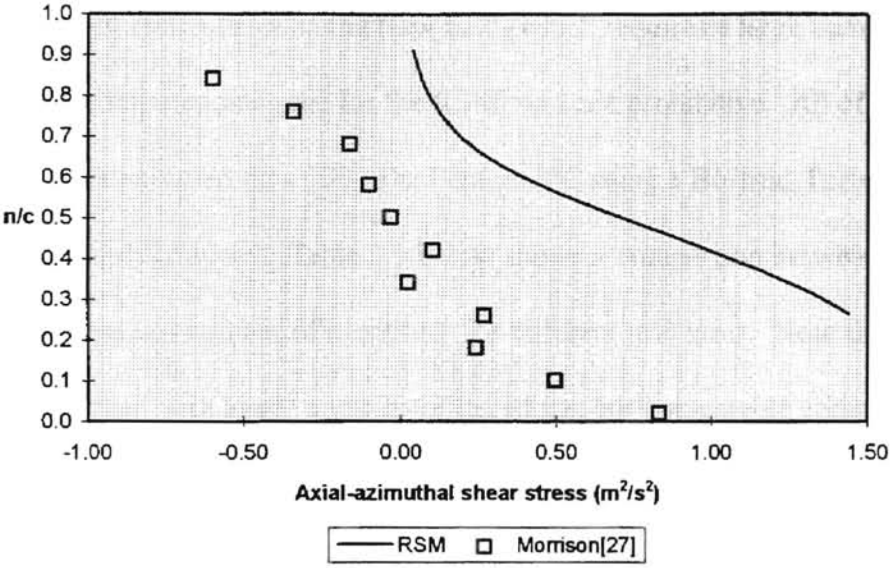

Figure 3.34. Comparison of radial-azimuthal Reynolds shear stress data at X/C=29.5

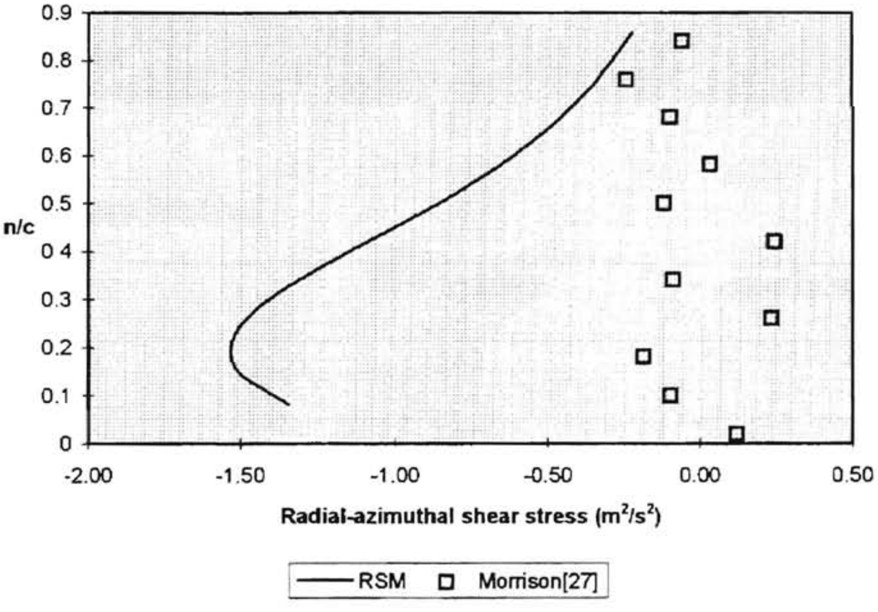

### 3.3 Computation time

Due to the lack of recirculation in the flow field (which requires a large number of iterations), the computational time for the RSM was not prohibitive. All of the calculations were executed on a 100 Mhz Pentium PC using a Borland Turbo C++ compiler optimized for speed. Table 3.1 below shows a comparison between the computation times and number of iterations for different grid sizes. Note that the larger grid sizes converged with lower numbers of iterations, but comparable computational times. The model under-relaxation methods were increased 30% for the 15x15 grid to prevent the solution from diverging. Figures 3.35-3.37 below show the residuals of 10 of the transport equations for three of the grid sizes examined (20x20, 30x20, and 40x20). As can be seen the $\overline{u^2}$ residual was the slowest to converge in all three cases, especially in the 20x20 grid case.

Table 3.1. Computation time

| Grid size | # of iterations | computational time (secs) |
|---|---|---|
| 15x15 | 262 | 49 |
| 20x20 | 337 | 88 |
| 30x20 | 151 | 77 |
| 40x20 | 149 | 117 |

Figure 3.35. Convergence of residuals
20x20 grid

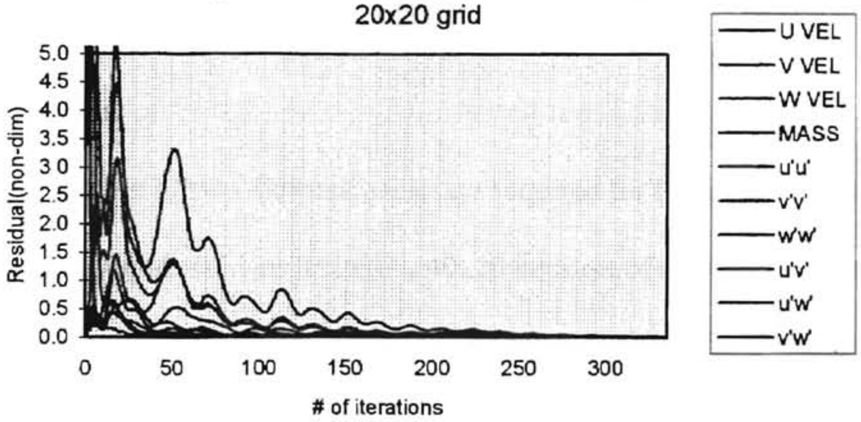

Figure 3.36. Convergence of residuals
30x20 grid

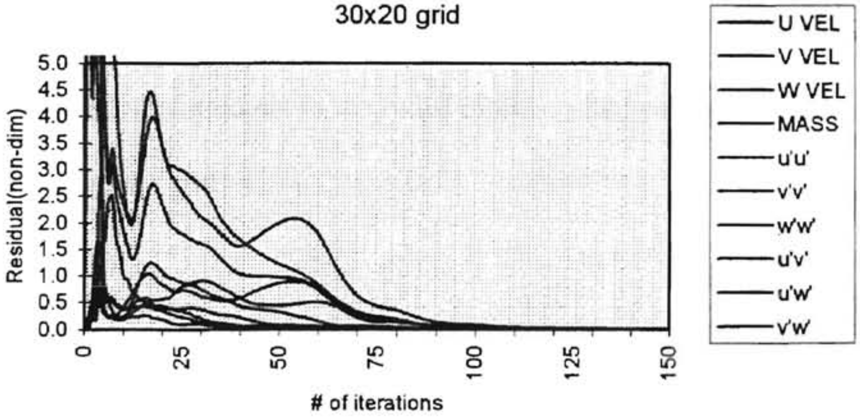

Figure 3.37. Convergence of residuals
40x20 grid

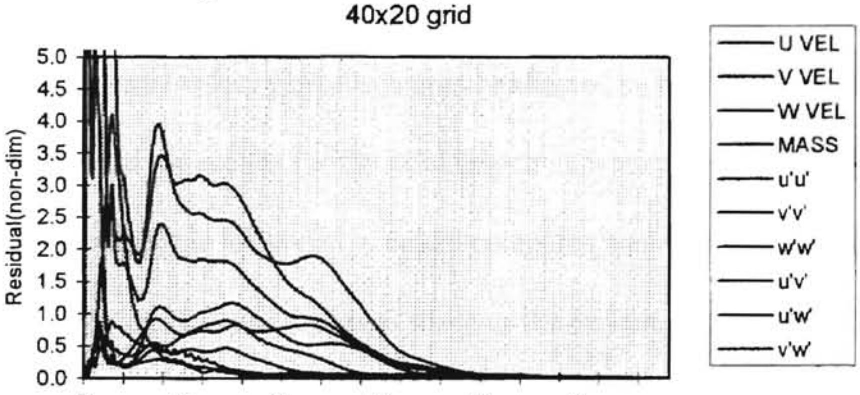

### 3.4 Grid dependence

Due to the large number of two dimensional arrays required for the RSM (35 vs only 16 for k-ε) the maximum grid size was limited to 40x20 because of memory constraints. This was only possible after 25 of the arrays were dynamically allocated locally instead of being stored as global arrays. All of the results shown above were made using a 20x20 uniform grid. The 40x20 grid size did not improve the comparison with the published experimental data over the 20x20 grid. The model will not converge for grid sizes smaller than 15x15 due to the large W velocity gradient in the radial direction that causes the $\overline{vw}$ equation to diverge with this coarse a grid.

### 3.5 Sumary of Results

Overall, the RSM does only a mixed job of predicting the values published from the laser Doppler anemometer experiment. The largest discrepancy of concern is the axial velocity profiles. The RSM appears to overpredict the viscous drag of the walls on the fluid. As mentioned above, the axial velocity profile is greatly affected by the specified volumetric flowrate. The RSM and k-ε results for the axial velocity are very similiar for x/c=5 and 13 but not x/c=29.5. Neither the RSM or k-ε model compares well with the experimental data at x/c=29.5. The k-ε data has the same shape as the experimental data, but lower values. This is somewhat strange since the axial flowrate is fixed. The only explanation is that the k-ε values immediately close to the walls are too large, this causes the values in the center of the channel to be below the experimental data. In summary, the k-ε model underpredicts the viscous drag immediately close to the wall because it cannot predict the anisotropic nature of the flow and the RSM overpredicts the viscous drag. Both the RSM and k-ε models do a good job of predicting the azimuthal velocity profiles.

The RSM does a good job of predicting the azimuthal normal stresses. Comparisons between the RSM and the published experimental data for the radial normal stress and axial-radial shear stress cannot be made without an in-depth look into why the published experimental data for these two quantities contradicts what appears to be logical assumptions. Likewise, this affects the $\overline{uw}$ and $\overline{vw}$ data as well.

The geometry could be modeled as a two velocity problem without much loss in computational accuracy. The values of V are so low in comparison to the U and W values throughout the flow that they do not have a substantial effect.

# CHAPTER IV

# CONCLUSIONS AND RECOMMENDATIONS

## 4.1 Conclusions

Agreement between the computational and published data varies in quality. The published experimental axial mean velocity (U) profile at the exit is very similar to fully developed turbulent channel flow. The RSM data shows that the U velocity profile is more laminar like. The radial mean velocity (V) is negligible throughout the seal. The centerline azimuthal velocity (W) continues to increase along the length of the seal. The azimuthal velocity profile is almost linear at the exit. This is confirmed by both the published experimental and RSM data. The published experimental data shows that the radial normal turbulent shear stress is the most dominant. In comparison, the RSM shows that the azimuthal normal stress is the most dominant. Overall levels of turbulence energy do correlate between the experimental and computational data. The axial-radial turbulent shear stress is the most dominant of all the turbulent shear stresses. This is confirmed by both the experimental and computational data. As would be expected , the computational data predicts a sign change in the axial-radial turbulent shear stress at the same location as the change in the slope of the axial velocity profile. This change in sign is not shown in the published experimental data.

It is believed that the principal reasons for the differences between the RSM predictions and the published experimental data is the boundary conditions for the Reynolds stresses at the rotating wall. All of the boundary conditions used are extended from k-ε models where the total wall shear stress is proportional to the total turbulent kinetic energy adjacent to the wall. Obviously for this type of flow, the individual wall shear stresses (i.e. $\tau_{xr}$, $\tau_{zr}$, and $\tau_{zx}$) have large differences in magnitude and are not all equally proportional to the total turbulent kinetic energy. This has been accounted for to some degree (see section 2.5.4), but only in a very empirical method.

### 4.2 Recommendations

The following recommendations can be made to improve the accuracy and applicability of the RSM to annular seals:

1. Improve the boundary condition at the rotating wall for all of the turbulence quantities. A method to correlate the relationship between the normal stresses and the three different wall shear stresses would improve the performance of the RSM near the rotating wall.
2. Implement wall reflection terms in the production terms for the turbulence quantities[11,19]. This may improve the comparison between the RSM and published data by allowing the normal stresses to interact more.
3. Apply this method to a full three dimensional model that does not assume the inner annulus is centered. This will be more difficult computationally, but will provide results that are more applicable to industry.

4. Apply this method to labyrinth seals. The Reynolds stress turbulence models could possibly predict the axial and azimuthal velocity profiles better in the labyrinth cavities than the eddy viscosity models used to date.

# REFERENCES

1. Anderson, D.A., Tannehill, J.C., and Pletcher, R.H., Computational Fluid Mechanics and Heat Transfer, Hemisphere Publishing, New York, 1984.

2. Childs, D., Turbomachinery Rotodynamics, John Wiley & Sons, New York, 1993.

3. Dietzen, F.J., and Nordmann, R., "Calculating Rotordynamic Coefficients of Seals by Finite Difference Techniques," University of Kaiserslautern, Kaiserslautern, Federal Republic of Germany, 1987.

4. Demko, J. A., The Prediction and Measurement of Incompressible Flow in a Labyrinth Seal. Ph. D Thesis, Texas A&M University, 1986.

5. Fu, S., Launder, B.E., and Leschziner, M.A., "Modeling Strongly Swirling Recirculating Jet Flow with Reynolds-Stress Transport Closures, " *Proceedings of the Sixth Symposium of Turbulent Shear Flows*, Toulouse, 1987, p.6.17.1.

6. Fu, S., Huang, P.G., Launder, B.E., and Leschziner, M.A., "A Comparison of Algerbraic and Differential Second Moment Closures for Axisymmetric Turbulent Shear Flows With and Without Swirl," *Transactions of the ASME*, vol. 110, 1988, pp. 216-221.

7. Gerald, C.F., and Wheatley, P.O., Applied Numerical Analysis, Addison-Wesley Publishing, Reading, MA, 1992.

8. Hanjalic, K., "Two Dimensional Flow in an Axisymmetric Channel," Ph.D thesis, University of London, 1970.

9. Hanjalic, K., and Launder, B.E., "A Reynolds Stress Model of Turbulence and its Application to Thin Shear Flows," *Journal of Fluid Mechanics*, vol. 52, 1972, pp. 609-638.

10. Hinze, J.O., Turbulence, McGraw-Hill, New York, 1975.

11. Huang, P.G., "The Computation of Elliptic Turbulent Flows with Second-Moment Closure Models," Ph. D thesis, Dept. of Mechanical Engineering, University of Manchester Institute of Science and Technology, 1986.

12. Huang, P.G., "Comment on 'Application of Wall Functions to Generalized Nonorthoganal Curvilinear Coordinate Systems' ,"*AIAA Journal*, vol. 33, 1995, pp. 2445-2446.

13. Huang, P.G., and Bradshaw, P., "Law of the Wall for Turbulent Flows in Pressure Gradients,"*AIAA Journal*, vol. 33, 1995, pp. 624-632.

14. Huang, P.G., and Coakley, T.J., "An Implicit Navier-Stokes Code for Turbulent Flow Modeling,"AIAA 30th Aerospace Sciences Meeting and Exhibit, Reno, NV, 1992.

15. Huang, P.G., and Coakley, T.J., "Modeling Hypersonic Flows with Second-Momement Closure,"*Near-Wall Turbulent Flows*, 1993, pp. 199-208.

16. Jones, W.P., and Pascau, A., "Calculation of Confined Swirling Flows with Second Moment Closure", *Journal of Fluids Engineering*, vol. 111, 1989, pp. 248-255.

17. Kubo, I., and Gouldin, F.C., "Numerical Calculations of Turbulent Swirling Flow," *Journal of Fluids Engineering*, 1975, pp. 310-315.

18. Landahl, M.T., and Mollo-Christensen, E., Turbulence and Random Processes in Fluid Mechanics, Cambridge University Press, New York, 1992.

19. Launder, B.E., Reece, G.J., and Rodi, W., "Progress in the Development of a Reynolds-Stress Turbulence Closure," *Journal of Fluid Mechanics*, vol. 68, 1975, pp. 537-566.

20. Launder, B.E., Priddin, C.H., and Sharma, B.I., "The Calculation of Turbulent Boundary Layers on Spinning and Curved Surfaces," *Journal of Fluids Engineering*, 1977, pp. 231-239.

21. Leonard, B.P., "A Stable and Accurate Convective Modeling Procedure Based on Quadratic Upstream Interpolation," *Computer Methods in Applied Mechanics and Engineering*, vol. 19, 1979, pp. 59-98.

22. Leschziner, M. A., "Modeling Strongly Swirling Flows with Advanced Turbulence Closures," *Proceedings of the First ASME-JSME Fluids Engineering Conference*, ASME FED, vol. 117, 1991.

23. Leschziner, M.A., "Refined Turbulence Modelling for Engineering Flows," ECCOMAS 94, John Wiley & Sons, 1994.

24. Lien, F.S. and Leschziner, M.A., "Modeling 2D and 3D Separation from Curved Surfaces with Variants of Second-Moment Closure Combined with Low-Reynolds Number Near-Wall formulation," *9th Int. Turbulent Shear Flow Symposium*, Kyto, Japan, 1993.

25. Lilley, D.G., Computational Fluid Dynamics, Dept of Mechanical and Aerospace Engineering, Oklahoma State University, Stillwater, OK, 1992

26. Lilley, D.G., and Rhode, D.L., "A Computer Code for Swirling Turbulent Axisymmetric Recirculating Flows in Practical Isothermal Combustor Geometries," NASA CR-3442, 1992.

27. Morrison, G. L., Johnson, M.C., and Tatterson, G.B., "Three-Dimensional Laser Anemometer Measurements in an Annular Seal," *Journal of Tribology*, vol. 113, 1991, pp. 421-427.

28. Morrison, G.L. , Johnson, M.C., and DeOtte, R.E., "Experimental Investigation of an Eccentric Labyrinth Seal Velocity Field using 3-D Laser Doppler Anemometry," Mechanical Engineering Dept., Texas A&M University, College Station, TX, 1992.

29. Patankar, V.S., Numerical Heat Transfer and Fluid Flow, Hemisphere Publishing, New York, 1980.

30. Pope, S.B., "The Calculation of Turbulent Recirculating Flows in General Orthogonal Coordinates," *Journal of Computational Physics*, vol. 26, 1978, pp.197-217.

31. Pope, S. B., and Whitelaw, J.H., "The Calculation of Near Wake Flows," *Journal of Fluid Mechanics*, vol. 73, 1973.

32. Rhode, D.L., Hensel, S.J., and Guidry, M.J., "Three-Dimensional Computations of Rotordynamic Force Distributions in a Labyrinth Seal," *Tribology Transactions*, vol. 36, 1993, pp. 461-469.

33. Schlichting, H., Boundary Layer Theory, McGraw-Hill, New York, 1960.

34. So, Ronald M.C., and Mohammad, N., "On the Modelling of Non-Reactive and Reactive Turbulent Combustor Flows," NASA CR-4041,1987.

35. Sloan, D.G., Smith, P.J., and Smoot, L.D., "Modeling of Swirl in Turbulent Flow Systems," *Prog. Energy Combust. Sciences*, vol. 12, 1986, pp. 163-250.

36. Stoff, H., "Incompressible Flow in a Labyrinth Seal", Journal of Fluid Mechanics, vol. 100, 1980, pp. 817-829.

37. Vance, J., Rotordynamics of Turbomachinery, John Wiley & Sons, New York, 1987.

38. White, F.M., Viscous Fluid Flow, McGraw-Hill, New York, 1991.

39. Wilcox, D.C., Turbulence Modeling for CFD, DCW Industries, La Canada, CA, 1993.

2

# VITA

Wallace Edward Wilcox

Candidate for the Degree of

Master of Science

Thesis: SECOND MOMENT TURBULENCE MODEL OF FLOW THROUGH A ROTATING ANNULAR SEAL

Major Field: Mechanical Engineering

Biographical:

Personal Data: Born in Conway, Arkansas on May 19, 1968, son of Wallace J. and Sandra L. Wilcox.

Education: Received a Bachelor of Science degree (Magna Cum Laude) from University of Missouri-Rolla in 1990; completed requirements for the Master of Science degree at Oklahoma State University in May, 1997.

Professional Experience: Specialist Engineer, CONOCO, Inc, December, 1990 to December, 1995; Reliability Engineer, CITGO, Inc., December 1995 to present; Registered Professional Engineer in the state of Oklahoma, Certified Vibration Specialist II.

Professional Membership: Vibration Institute